

Design of Compliant Meanders for Applications in MEMS, Actuators, and Flexible Electronics

Bavani Balakrisnan¹, Aleksandar Nacev², Jeffery Burke², Abhijit Dasgupta¹, Elisabeth Smela^{1*}

¹Department of Mechanical Engineering, 2176 Glenn L. Martin Hall

²Department of Bioengineering, 2314 Kim Building,
University of Maryland, College Park, Maryland 20742

*email: smela@umd.edu, tel: 301-405-5265

Abstract

Meandering beams, crenellated surfaces, and zigzag-shaped electrodes are employed as compliant elements in micro-scale applications ranging from springs attached to proof masses in micro-electro-mechanical systems (MEMS) to stretchable electrodes in flexible electronics and dielectric elastomer actuators. An understanding of how the meander shape affects the stiffness of these structures would permit preliminary design without the necessity of fabricating or running simulations on each case. In this paper, we present general guidelines for designing meandering cantilevers, showing how the amplitude, angle, length, and thickness affect both the axial and bending stiffnesses. Simple analytical expressions are derived, and the results are compared with those from numerical simulations and experimental measurements. The more complex case of a stiff thin film overlying a crenellated elastomer is also simulated.

Keywords: axial stiffness, bending stiffness, stretchable electrode, corrugated, crenellated, analytical model, FEM, design

1 Introduction

Meandering paths are widely used to decrease the stiffness of mechanical structures, including inplane zigzags or serpentes and out-of-plane crenellation or corrugation. This allows one to retain desired properties, such as the high conductivity of a metal or high strength of silicon, without having to employ another material of substantially lower modulus that may not have the same performance or compatibility with standard fabrication methods. For example, meandering polysilicon paths have been used to create springs to tether proof masses in microresonators [1], tunable capacitors[2], and RF switches [3].

Meander paths and crenellation are also often used to form stretchable electrodes from metal films, which are required in flexible displays [4], stretchable circuits [5], flexible antennas [6], and dielectric elastomer actuators (DEAs) [7]. (Patterned metals, unlike some other compliant electrodes, have the advantage of compatibility with standard microfabrication processes). The metal is typically deposited onto a supporting compliant substrate. For example, the rupture strain (ductility) of a single crystal Au film is 1-1.5% [8]; however, patterning the metal films inplane allows it to undergo strains of up to 100% without rupture [10-14] and with minimal change in conductivity [13]. Patterning in-plane is typically achieved by photolithography [15], while out-of-plane deformation has been produced by molding the surface [16] or by depositing a metal onto a stretched substrate that is later relaxed to form wrinkles [17].

The stiffness of crenellated structures has previously been obtained by summing up, in parallel or in series, the stiffness of each individual segment, obtained using the expression for the stiffness of a cantilever [2,18]. This can, however, under- or over-estimate the stiffness [3] because the interaction among segments is not considered. A closed-form analytical solution for the specific case of a rectangular crenellated cantilever with guided-end boundary conditions has been derived [1]. Numerical simulations have been performed for specific shapes (rectangular, trapezoidal, sinusoidal) under specific boundary conditions (such as both ends fixed, or one end fixed and the other end guided) [1,3,19]. However, extrapolation to other geometries requires new simulations. Thus, while the stiffness of a limited number of crenellated shapes has been studied analytically [1], numerically [19,20], and experimentally [1], a design guide exploring the effects of the meander shape has not been presented.

In order to facilitate the evaluation of the effects of the design parameters, this paper determines the axial and bending stiffness of meandering cantilevered structures (one end fixed and the other free) as a function of their geometry (Figure 1), where stiffness (given by the spring constant k) was found from the force required to achieve a unit displacement (or vice versa). The basic unit making up the beam structures (Figure 1b) considered in this study comprises two sides of a trapezoid, as shown in Figure 1a. The key parameters varied in this investigation were the tilt angle α measured from the horizontal, the amplitude A , and the length of the horizontal segment H . When $\alpha = 90^\circ$ a square wave results from concatenating these basic units, and for $H = 0$, a triangle wave is formed. Other shapes considered in this study were sinusoidal and sawtooth.

To permit rapid estimation of the axial and bending stiffnesses and to understand how the various parameters affect them, simple analytical expressions that account for the dominant contributions to stiffness have been derived based on classical beam theory. The stiffness was also determined using 2D numerical simulations, and the results are within 6% of each other for axial stiffness and 10% for bending stiffness. Thus, despite their simplicity, the analytical models are surprisingly accurate, and they can be readily used to approximate the stiffness of various shapes without the need for FEM. In addition, the values for several of the shapes were validated experimentally.

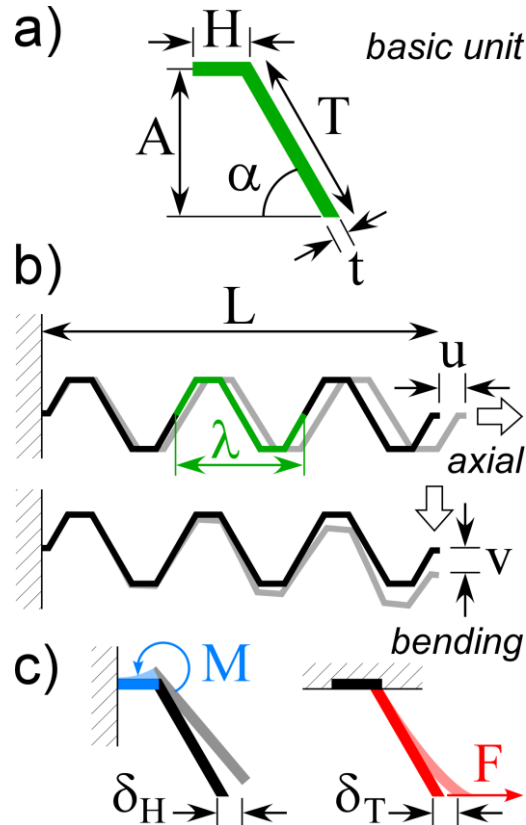


Figure 1. a) Parameters defining the beam geometry. b) A trapezoidal example of the 3-period beams used in this work. The fixed-free boundary conditions and the axial and bending displacements are indicated. c) Schematic illustration of the primary deformations of the horizontal (blue) and tilted (red) segments of the basic unit during axial elongation

induced by an applied force F in the axial direction. (left) Horizontal component δ_H of deflection due to a moment M acting on the horizontal segment (blue). (right) Horizontal component δ_T of deflection due to bending of the tilted segment (red). See section 3.1 for details.

The first key parameter that was varied was the tilt angle α . We show that the axial and bending stiffness both decrease with α : the axial stiffness k_x dropping by a factor of 4 and the bending stiffness k_y by a factor of 2 as α increases from 45° to 120° . Secondly, the amplitude A was varied for a rectangular crenellation ($\alpha = 90^\circ$). The axial stiffness decreases strongly with crenellation height, being proportional to $1/A^3$, while k_y is less affected, being proportional to $1/A$. We also find that axial stiffness is unaffected by the addition of horizontal segments at the vertical center, but their addition off the vertical center lowers k_x (Section 3.5). Bending stiffness depends instead on the overall length of the structure, not the vertical position of additional horizontal segments.

Lastly, using numerical simulations we examined the more complex case of a thin film overlying an out-of-plane-corrugated elastomer of varying thickness (Section 3.6). Such structures are found in compliant electrodes [16] and dielectric elastomer actuators [16,21]. We show that for this “filled” structure, at $2A = 0$ (no crenellation) the axial stiffness of the filled structure is approximately equal to that of the metal film. Increasing the crenellation amplitude reduces the axial stiffness by orders of magnitude until it reaches the elastomer stiffness. The bending stiffness for the filled structure with $2A = 0$ is already close to that of the elastomer alone. It initially increases somewhat with crenellation amplitude, reaches a maximum, and then decreases until it levels off at the elastomer stiffness. Crenellation therefore has only a minor effect on bending stiffness, but if it is to be used, care must be taken in designing the crenellation to achieve the desired value.

2 Methods

In the simulations, the stiffness was determined by subjecting each structure to a known displacement (axial displacement u or bending displacement v , Figure 1b) and calculating the reactive force, F . For the analytical estimates, a force, F , was applied to the structure and the total displacement, δ , due to deformations of the vertical and horizontal segments was found using basic beam theory.

2.1 Numerical Simulations

The numerical simulations were developed using COMSOL Multiphysics version 3.5a, a finite element modeling tool. The 2D structural mechanics plane-stress application mode was used with free triangular meshing and assuming small static prescribed deflections. In the plane-stress mode, the z -components of the stress tensor are assumed to be zero and the loads are constant throughout the width of the material. More detailed information about the model can be found in the Supplementary Information.

The left end boundary of the structure was fixed, and a small prescribed displacement (well below the elastic limit) was applied at the right end of the corrugated beam (Figure 1b). For determining axial stiffness, the displacement u was $1 \mu\text{m}$. The reaction force in the x -direction was determined by integrating the reaction force at the right hand boundary. The reaction force divided by the prescribed displacement gave the axial stiffness. (The boundary condition was such that the reaction force in the y -direction was zero, so the beam could deflect freely in the y -direction.) Similarly, the bending stiffness was determined by applying a $1 \mu\text{m}$ displacement v perpendicular to the tip of the cantilever and determining the reaction force in the y -direction. (The boundary condition was such that the reaction force in the x -direction was zero, allowing the cantilever to deflect freely in x -direction). Model validation was conducted on a straight cantilever beam (see Supplementary Information). The axial and bending stiffnesses, k_x and k_y , were normalized by the width of the beam and the elastic modulus of the material, so they are dimensionless

$$\left(\frac{N/m}{m \cdot Pa} \right).$$

For crenellated elastomeric (low modulus) structures with an overlying high-modulus thin film, the modulus of the elastomer was kept constant at 1 MPa and the modulus of the electrode was varied from 5 to 100 GPa. The clamped left side of the structure was kept fixed, and on the free right side equal displacement was applied to both materials. The stiffness was obtained as described above. Because two materials were used in these structures, it was not possible to normalize by the modulus, so the combined beam stiffness was instead normalized by the width of the beam and the stiffness units are N/m².

2.2 Experimental Methods

Using a paper printout stencil, a 0.8 mm diameter copper (Cu) wire was manually bent using pliers to the desired angles to give a structure of three periods, as shown in Figure 1a and as used in the simulations. Each period λ was 8 cm long, making $L = 24$ cm. The length to thickness ratio was $L/t = 300$ to allow the results to be readily compared to the simulations. Bulk Cu has a modulus $E = 120$ GPa [22]. In order to compare the experimental results to the analytical and numerical models, the 800 μm diameter wire was treated as a square beam with thickness $t = \text{width } w = 800 \mu\text{m}$.

For axial stiffness testing, the Cu wire was fixed vertically at the top, weights (5, 10, 20, 30, 40 g) were hung at the bottom, and the deflections were recorded. The wire was unloaded between tests to confirm the absence of permanent deformation (that the loading was within the elastic regime). The stiffness was found from the slope of the load-deflection plot. For bending stiffness testing, the Cu wire was fixed horizontally on the left side and weights were hung on the right side. Because larger deflections were observed, smaller weights were used (0.28, 0.56, 0.84, 1.12, 1.4 g). (For a picture of the experimental setup, further details, and the displacement data, see Supplementary Information)

3 Results

3.1 Analytical Estimation of Axial Stiffness

To estimate the axial stiffness of the trapezoidal beams, the deflection of a single unit (Figure 1a) was found using beam theory, and the total deflection was obtained by multiplying the deflection of the unit by the number of units. (A more detailed derivation is given in the Supplementary Information.) Briefly, the applied force F produces a moment $M = A \times F$ on the horizontal segment of the unit, H, where A is the amplitude, or distance of segment H above the center line, and is the length of the moment arm. This causes H to bend, angling the vertex connected to the tilted segment, T, by θ_H [23]:

$$(1) \quad \sin \theta_H = \frac{MH}{EI} = \frac{FAH}{EI} ,$$

where θ_H is given in radians, H is the length of horizontal segment H, E is the Young's modulus of the material, and I is the moment of inertia of the segment. Thereby, the tilted segment T is rotated, deflecting the tip of T by δ_H (Figure 1c):

$$(2) \quad \delta_H = A \sin \theta_H = \frac{FA^2H}{EI} .$$

The tilted segment T is treated as a cantilever beam fixed at the top end. A force F applied at the tip of a cantilever generates a deflection δ_T given by [23]:

$$(3) \quad \delta_T = \frac{FT^3}{3EI} = \sin \alpha \frac{F \cos(\theta_H + 90 - \alpha) \left(\frac{A}{\sin \alpha}\right)^3}{3EI},$$

where T is the length of segment T.

Summing the two deflections, $\delta = \delta_H + \delta_T$, taking the stiffness $k_x = F/n\delta$, where n is the number of periods in the beam, and using $I = wt^3/12$ for a rectangular cross section, the axial stiffness of the beam is given approximately by:

$$(4) \quad k_x = \frac{Ewt^3}{12nA^2 \left(H + \frac{A \cos(\theta_H + 90 - \alpha)}{3(\sin \alpha)^2} \right)}$$

3.2 Analytical Estimation of Bending Stiffness

A reasonable analytical estimate of the bending stiffness requires a more complex treatment than the one for the axial stiffness because the moment arm is not constant throughout the beam but depends on the distance of the segment from the end and because terms that were neglected above are not insignificant here. Deflections and rotations caused by both force and moment must be considered. Figure 2 shows the various segments and dimensions in the meander.

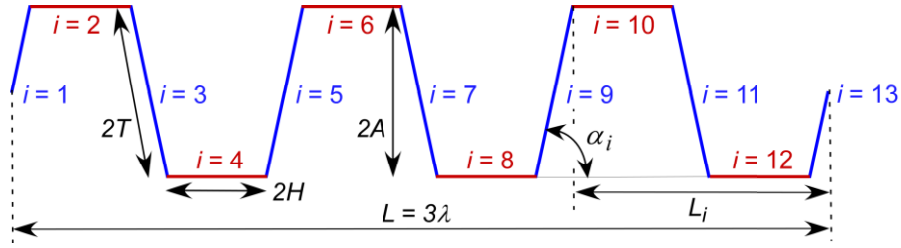


Figure 2. Schematic of a meander structure with $n = 3$ periods of length λ showing the numbering of the segments as well as the angle and moment arm for segment $i = 9$.

Before the structure is subjected to a force at the tip, the length of the moment arm for the i^{th} horizontal segment is:

$$(5) \quad L_i = L + \left[\frac{A}{\tan \alpha_i} - \frac{i}{2} \frac{L}{2n} \right], \quad i = \text{even (horizontal segments)}$$

where n is the number of periods and the length of the first segment is $T \cos \alpha_1 = A / \tan \alpha_1$ since $A = T \cos(\alpha_1 - 90) = T \sin \alpha_1$. In what follows, the L_i are assumed not to change significantly during bending, which is valid for small deflections. The length of the moment arm for the i^{th} vertical or tilted segment is:

$$(6) \quad L_i = L - \left[\frac{A}{\tan \alpha_i} + \frac{(i-1)}{2} \frac{L}{2n} \right], \quad i = \text{odd (vertical segments)}$$

except for $i = 13$, for which it is zero because the moment at the end of the beam is zero.

Each segment contributes four components to the deflection (Figure 3). This is illustrated for an arbitrary segment i of length B_i at an angle α_i . The segment is treated as if it is rigidly attached on the left side. For simplicity, the portion of the meander to the right of the segment is represented as a horizontal line. Figure 3a shows the position before the force is applied. The total deflection at the tip is found by summing the four contributions.

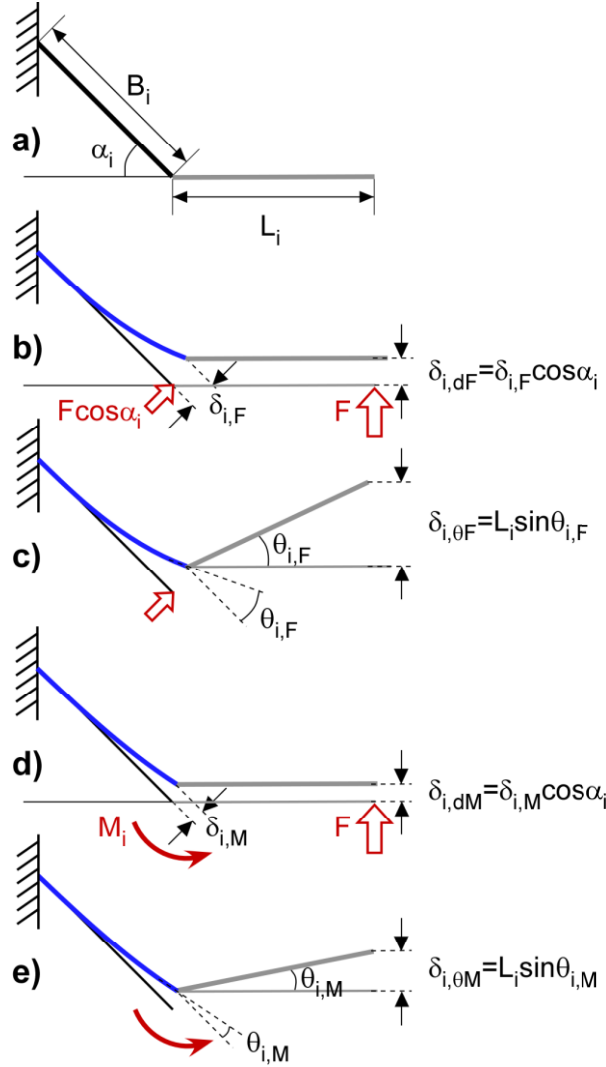


Figure 3. Illustration of the four contributions to the deflection at the rightmost tip of the structure from a beam segment of length B_i rigidly mounted on its left and attached to a horizontal section of length L_i . a) Before application of the force at the tip. b) Deflection $\delta_{i,F}$ at the tip of the segment due to segment bending caused by the component of force perpendicular to the endpoint of the segment and the resulting deflection $\delta_{i,dF}$ at the endpoint. c) Tilt of the horizontal section due to the bending angle $\theta_{i,F}$ arising from the bending in (b). d) Deflection due to beam bending caused by the moment M on the segment. e) Tilt of the horizontal section due to the bending angle $\theta_{i,M}$.

In response to a force perpendicular to the tip of the meander (Figure 3b), the segment will deflect as if it experienced a force $F \cos \alpha_i$ perpendicular to its endpoint, leading it to deflect an amount $\delta_{i,F}$ in that direction. This produces a deflection at the endpoint of the meander of

$$(7) \quad \delta_{i,dF} = \delta_{i,F} \cos \alpha_i,$$

where the subscript i indicates the segment number, d a contribution due to deflection, and F a contribution due to the force. The tip of the segment is rotated, as a result of the deflection, by an angle $\theta_{i,F}$, tilting the portion of the meander to its right by this angle (Figure 3c). The tilt results in a deflection at the meander endpoint of

$$(8) \quad \delta_{i,\theta F} = L_i \sin \theta_{i,F},$$

where the subscript θ indicates a tip deflection due to tilt.

The force at the tip of the meander furthermore results in a moment $M_i = F \times L_i$ on the segment. The moment also leads to a deflection of the segment (Figure 3d), this deflection having a magnitude $\delta_{i,M}$, where the subscript M indicates that the deflection is due to the moment. This appears at the meander endpoint as a deflection of magnitude

$$(9) \quad \delta_{i,dM} = \delta_{i,M} \cos \alpha_i.$$

This beam bending again causes the portion of the meander to the right of the segment to tilt (Figure 3e), and the meander endpoint to displace by

$$(10) \quad \delta_{i,\theta M} = L_i \sin \theta_{i,M}.$$

Beam theory was used to evaluate the four contributions [23]. The deflection due to force is given by

$$(11) \quad \delta_{i,F} = \frac{(F \cos \alpha_i) B_i^3}{3EI},$$

and the angle $\theta_{i,F}$ is given by

$$(12) \quad \theta_{i,F} = \frac{(F \cos \alpha_i) B_i^2}{2EI}.$$

The displacement $\delta_{i,M}$ is given by

$$(13) \quad \delta_{i,M} = \frac{M_i B_i^2}{2EI} = \frac{FL_i B_i^2}{2EI},$$

and, finally, the rotation due to moment is given by

$$(14) \quad \theta_{i,M} = \frac{M_i B_i}{EI} = \frac{FL_i B_i}{EI}.$$

The deflection at the tip of the meander due to segment i is found by summing the four terms.

$$(15) \quad \begin{aligned} \delta_i &= \delta_{i,dF} + \delta_{i,\theta F} + \delta_{i,dM} + \delta_{i,\theta M} \\ &= \frac{(F \cos \alpha_i) B_i^3}{3EI} \cos \alpha_i + L_i \sin \left(\frac{(F \cos \alpha_i) B_i^2}{2EI} \right) + \frac{FL_i B_i^2}{2EI} \cos \alpha_i + L_i \sin \left(\frac{FL_i B_i}{EI} \right) \end{aligned}$$

For small rotations, $\sin \theta_{i,F} \approx \theta_{i,F}$ and $\sin \theta_{i,M} \approx \theta_{i,M}$, allowing Equation (15) to be simplified as follows.

$$(16) \quad \begin{aligned} \delta_i &\approx \frac{(F \cos \alpha_i) B_i^3}{3EI} \cos \alpha_i + L_i \left(\frac{(F \cos \alpha_i) B_i^2}{2EI} \right) + \frac{FL_i B_i^2}{2EI} \cos \alpha_i + L_i \left(\frac{FL_i B_i}{EI} \right) \\ &= \frac{FB_i}{EI} \left[\frac{B_i^2 \cos^2 \alpha_i}{3} + L_i B_i \cos \alpha_i + L_i^2 \right] \end{aligned}$$

The total deflection at the tip of the cantilever is the sum over all the segments except the last ($i = 13$):

$$(17) \quad \delta = \delta_1 + \sum_{i=2}^{4n} \delta_i = \delta_1 + \sum_{i=odd, i=3}^{4n-1} \delta_{iT} + \sum_{i=even, i=2}^{4n} \delta_{iH},$$

where the subscripts H and T indicate the horizontal and vertical segments. The total number of segments is $4n$: $2n$ horizontal segments and $2n$ vertical segments.

If one takes into account changes in the angles α_i due to the tilt of segments to their left, then for $i > 1$:

$$(18) \quad \alpha_i = \alpha + \sum_{j=1}^{i-1} (\theta_{j,F} + \theta_{j,M})$$

However, a reasonable estimate can be obtained by treating α as constant. In that case, for $i = \text{odd}$ (tilted or vertical segments), $\alpha_i = \alpha$, and for $i = \text{even}$ (horizontal segments) $\alpha_i = 0$ and $\cos \alpha_i = 1$. For $i = 1$, $B_i = T$; for $i = \text{odd}$, $B_i = 2T$, and for $i = \text{even}$, $B_i = 2H$. In this case, we can write:

$$\delta = \frac{FT}{EI} \left\{ \left[\frac{T^2 \cos^2 \alpha_1}{3} + L_1 T \cos \alpha_1 + L_1^2 \right] + 2 \sum_{i=odd, i=3}^{4n-1} \left[\frac{(2T)^2 \cos^2 \alpha_i}{3} + 2L_i T \cos \alpha_i + L_i^2 \right] \right\} \\ + \frac{F(2H)}{EI} \sum_{i=even, i=2}^{4n} \left[\frac{(2H)^2}{3} + 2L_i H + L_i^2 \right]$$

(19)

The bending stiffness k_y is then given by:

$$(20) \quad k_y = \frac{F}{\delta} .$$

3.3 Beam Shape

The effect of beam shape for various trapezoidal configurations was investigated, varying α (and thereby simultaneously H); sinusoid and sawtooth shapes were also examined. The amplitude was fixed at $A = 25t$, where $t = 1 \mu\text{m}$ is the beam thickness, and for each beam, three periods of $100 \mu\text{m}$ length were used. (In the simulations, to ensure that the displacement was applied at the vertical midline, additional short horizontal sections $2.25 \mu\text{m}$ in length were affixed at each end making the total length of the beam $L = 304.5 \mu\text{m}$.) The smallest angle allowing that combination of A and L is $\alpha = 45^\circ$, and the largest angle that gives a shape for which the line does not cross itself is 130° ; we stopped at 120° . (Although not shown here, while the stiffness values vary with t , the dependence of stiffness on α is unvarying with t .) It should be noted that axial tension in the x -direction causes a comparable size displacement in the y -direction.

Table 1. Stiffness of beams with a length of three periods, amplitude $A = 25t$, and varying shapes, normalized to the stiffness of a straight beam of the same length and thickness.

Shape				Relative k_x			Relative k_y		
Type	α (deg)	H (μm)	Schematic	FEM	Estimate	† Expt.	FEM	Estimate	Expt.
Straight Beam	0	---		1.00	1.00	---	1.00	1.00	1.00
				below, $\times 10^{-4}$			below, $\times 1$		
Trap (triangle)	45	0.0		2.90	2.87	2.45	0.72	0.71	0.62
Trap	49	6.5		2.37	2.36		0.70	0.71	
Trap	56.5	16.7		1.85	1.84		0.66	0.67	
Sawtooth	90, 45	0.0		1.80	1.68		0.43		
Sinusoid	---	---		1.72	---		0.64		
Trap	63.4	25.0		1.56	1.55		0.63	0.63	
Trap	76	37.5		1.24	1.24		0.57	0.57	
Trap (rectangle)	90	50.0		1.00	1.01	1.00	0.51	0.50	0.41
Trap	104	62.5		0.86	0.85		0.46	0.43	
Trap	110	68.2		0.80	0.79	0.75	0.42	0.40	0.34
Trap	120	78.9		0.70	0.69		0.37	0.34	

† Experimental axial values are normalized to the rectangle value, which was set to 1×10^{-4} .

Note: For the dimensions used in the simulations ($L = 300 \mu\text{m}$, $t = 1 \mu\text{m}$), the axial stiffness (per unit modulus and unit width) of the rectangular trapezoid was $3.3 \times 10^{-7} \text{ (N/m)/(m}\cdot\text{Pa)}$, and its bending stiffness was 4.5×10^{-9} , a factor of 75 smaller. The experimental axial stiffness of this shape was 17.7 N/m and the bending stiffness was 0.23 N/m , smaller by the same

The results of the simulations, analytical estimates, and experimental measurements are presented in Table 1 in order of decreasing axial stiffness, normalized by the stiffness of the straight beam to give a relative stiffness. For this amplitude, crenellation reduces the axial stiffness by four orders of magnitude. (The effect of varying amplitude is examined in the next section.) Bending is much less affected, being reduced in the best case by 63%.

3.3.1 Axial Stiffness

The agreement between the simulation, analytical, and experimental results for the axial stiffness k_x in Table 1 was good, as illustrated in Figure 4a. The difference between the FEM result and the analytical estimate was at most 1.5% except for the sawtooth, for which it was 6%. The difference between the experimental and analytical results was at most 3% except for the triangle, for which it was 15%.

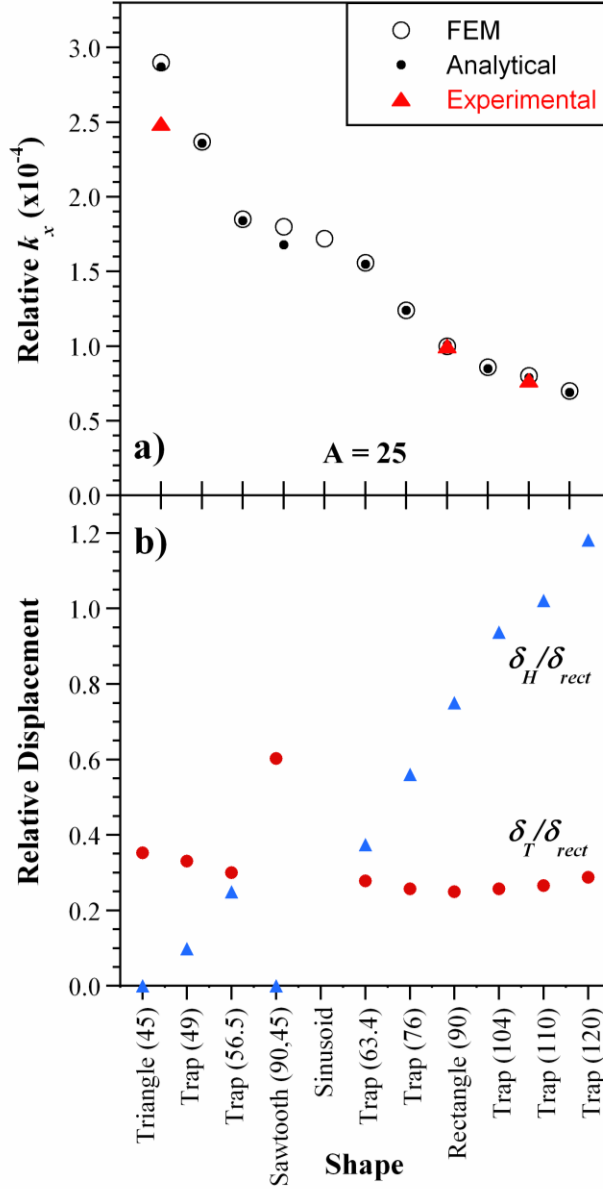


Figure 4. a) Axial stiffness relative to that of a straight beam as a function of corrugation angle for an amplitude $A = 25t$ found by simulation, analytical estimation, and experimentally. b) Displacement of the horizontal (δ_H) and vertical (δ_T) segments, normalized to the total axial displacement of the rectangle (δ_{rect}).

The relative stiffness decreases monotonically with angle α . The triangular shape ($\alpha = 45^\circ$) has the highest relative axial stiffness (2.9×10^{-4}), while the trapezoid with $\alpha = 120^\circ$ has the lowest (0.7×10^{-4}), a factor of four smaller. In comparison with the 10^{-4} drop in stiffness due to crenellation of this amplitude, this difference is relatively small. The rectangular shape is a good choice because it has one of the lowest stiffnesses and is typically the easiest to fabricate.

The reason for the dependence on α is elucidated in Figure 4b, which shows the contributions of the displacements δ_H and δ_T due to the horizontal and tilted segments relative to the total displacement of the rectangular shape. (I.e., Trap(49) has $\delta_H / \delta_{rect} = 0.1$, meaning that the axial displacement due to the horizontal segment is 10% as large as the total axial displacement of the rectangle. Trap(49) also has $\delta_T / \delta_{rect} = 0.33$, so its total axial displacement $\delta_H + \delta_T$ is 43% as large as for the rectangle.) The bending of the tilted segment is almost constant across the different shapes, but because of the increasing length of the horizontal segments for the shapes with larger α (δ_H depends linearly on

H by Equation (2), and H depends linearly on α , the relative contribution of δ_H to the total displacement increases with α . (Recall that a larger displacement under the same force means a lower stiffness.)

The axial stiffnesses of the sinusoidal and sawtooth beams lies between the trapezoids with α 56.5° and 63.5°. The sinusoidal case cannot be solved with our analytical model, but the sawtooth result was found by summing the contributions of the tilted and vertical components (for this shape, $H = 0$). The sawtooth is softer than the triangle, although both have $H = 0$, because it has greater number of segments (12 versus 6), giving a greater total length.

3.3.2 Bending Stiffness

There was also good agreement between the simulations, analytical results, and experiments for the bending stiffness k_y , as illustrated in Figure 5a. The difference between the FEM results and the analytical estimates was at most 10%. The difference between the experimental and analytical values was at most 18%. This discrepancy was primarily due to a systematic offset of the experimental values, which were uniformly lower by $15 \pm 2.5\%$. The trend, however, followed exactly as expected. The specimens for meander beam experiments were made by hand-bending the shapes, so the corners were rounded. This offset was more prominent in bending than in axial loading (compare Figure 4a) because the change in stiffness was smaller.

As for the axial stiffness, the bending stiffness relative to that of a straight beam decreases with α , from 0.72 at 45° to 0.37 at 120°. The decrease in bending stiffness of the meander is again due to the lower stiffness of the longer horizontal segments, which undergo greater deflection (Figure 5b). The bending stiffness of the sinusoidal structure follows the same trend, but the bending stiffness of the sawtooth is comparable to that of the rectangle.

Figure 5(c) shows the fraction of bending displacement contributed by each of the terms in Equation (15) for the vertical segments. The main contributing factor for the tilted segment is $\delta_{T,\theta M}$, the tilting of the cantilever due to the moment, and the contribution of this term increases with α . Although this term looks large and the other 3 terms small, ignoring the other 3 terms gives large percentage of error when comparing different shapes. The terms $\delta_{T,dM}$ and $\delta_{T,\theta F}$ are the same magnitude, and they decrease with α , going to zero for the rectangle ($\alpha = 90^\circ$) and then going negative (i.e., causing a deflection in the $-y$ direction). The term $\delta_{T,dF}$ decreases with α and also goes to zero for a rectangle, but then it slightly increases again for $\alpha > 90^\circ$. Since only the $\delta_{T,\theta M}$ contributes to the bending deflection for the rectangle, this simplifies the bending stiffness equation for that shape (see Equation (19)).

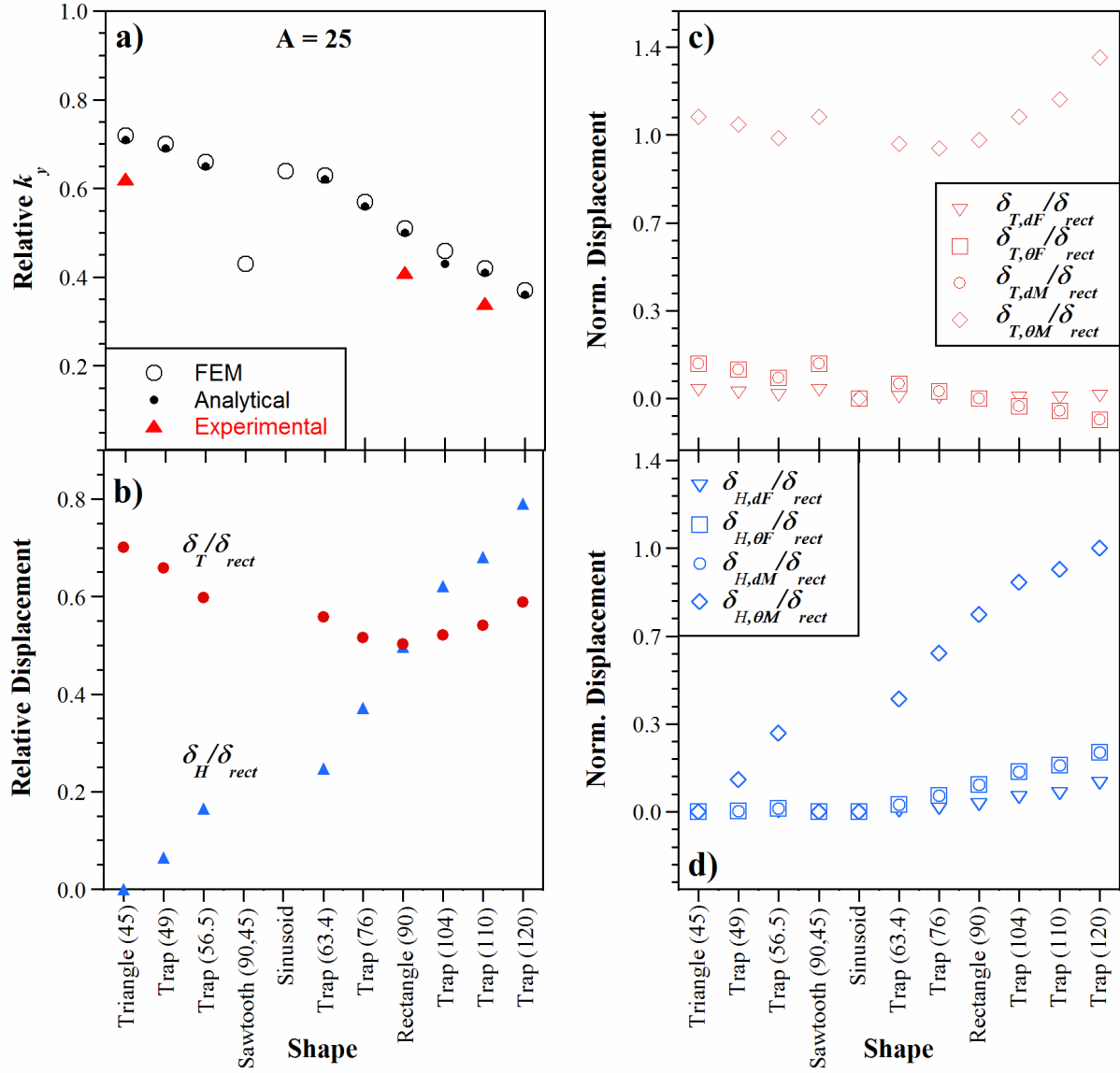


Figure 5. a) Relative bending stiffness as a function of corrugation angle for an amplitude $A = 25t$ found by simulation, analytical estimation, and experimentally, with the stiffness normalized to that of a straight beam. b) The fraction of bending displacement due to bending of the horizontal (δ_H) and vertical (δ_T) segments given by the analytical approach in (a), normalized by the total displacement of the rectangular crenellation. The relative contributions to (c) δ_T and (d) δ_H by each of the four terms again normalized by the total displacement of the rectangular crenellation.

Figure 5(d) shows the fraction of bending displacement contributed by each of the terms in Equation (15) for the horizontal segments. Since the triangle does not have the horizontal segment, all four terms are zero. Just as for the vertical segments, the main contribution is from $\delta_{H,\theta M}$, the tilting of the cantilever due to the moment. The terms $\delta_{T,dM}$ and $\delta_{T,\theta F}$ are again of comparable magnitudes. The term $\delta_{H,dF}$ contributes the least. Looking at this another way, increasing α increases H , and Equation (14), the largest contributor, increases linearly with H . This results in the bending stiffness actually being proportional to the total length of the structure (for a given A), as shown in Figure 6.

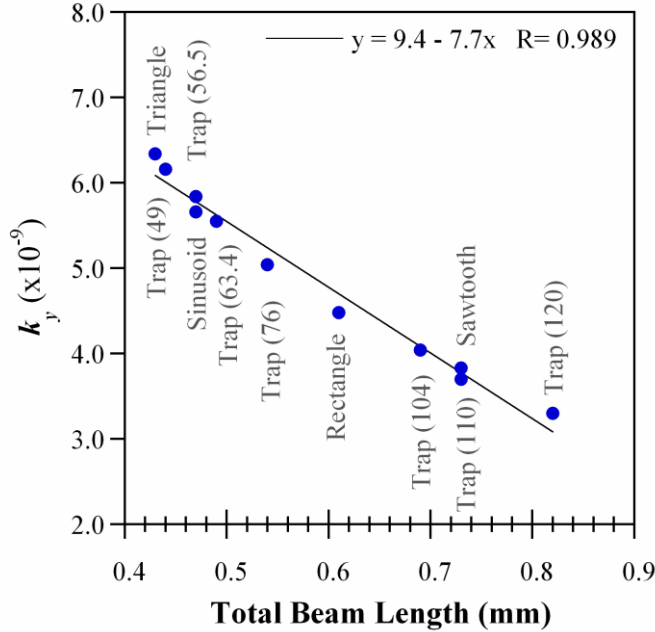


Figure 6. Bending stiffness (FEM values) versus the total beam length for the different shapes.

3.4 Effect of Amplitude

For $\alpha \neq 90^\circ$, the amplitude A will be limited by the period length. Only for a rectangular crenellation can A be increased without modifying the period. Here we consider, for the rectangular crenellation, the effect of amplitude on the bending and axial stiffness.

3.4.1 Axial Stiffness

By Equation (4), the most effective way to reduce the axial stiffness of the beam is to decrease its thickness t , since that comes in as the cube. For a given thickness, however, the most effective way to achieve a more compliant beam is to increase the amplitude of the meander or corrugation, A . Figure 7a shows the effect on the axial stiffness k_x of varying A for a rectangular crenellated beam ($\alpha = 90$, $H = 25$). The simulation results are shown together with the analytical estimate. For this case, the normalized axial stiffness is:

$$(21) \quad \frac{k_x}{Ew} = \frac{t^3}{144A^2 \left(H + \frac{A \cos(\theta_H)}{3} \right)} \approx \frac{t^3}{144A^2 \left(H + \frac{A}{3} \right)}$$

As usual, the amplitude is given in units of thickness and the stiffness is reported relative to that of an uncorrugated (straight) beam.

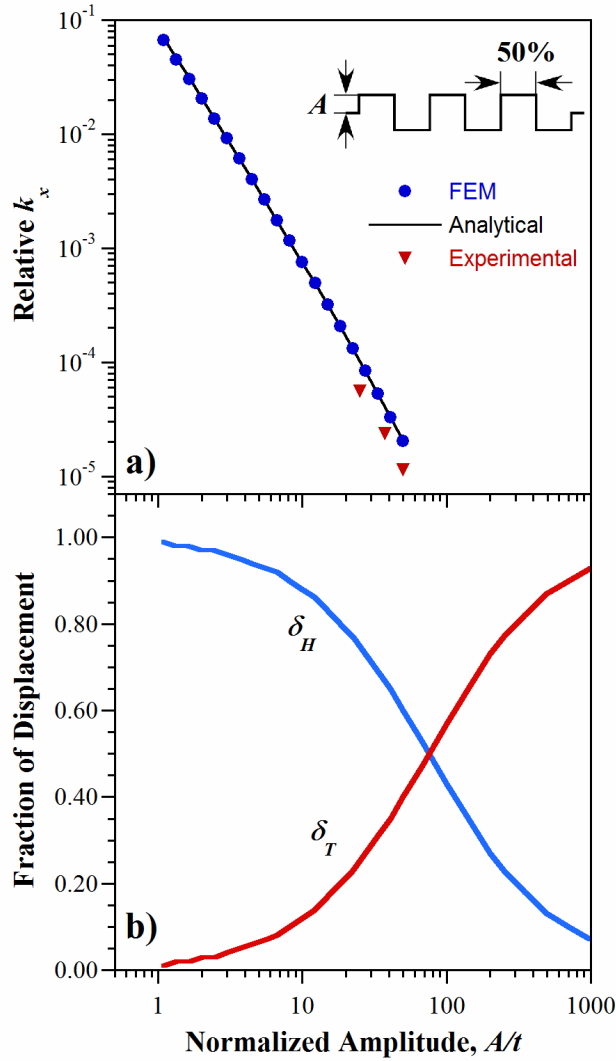


Figure 7. a) Axial stiffness (simulation, analytical estimation, and experimental) relative to that of a straight beam as a function of crenellation amplitude, where A is normalized by the beam thickness t . b) The fraction of axial displacement due to bending of the horizontal (δ_H) and vertical (δ_T) segments, given by the analytical approach.

Values from the FEM simulations and the analytical estimate were once again close. For $A = t$ (a crenellation amplitude equal to the beam thickness), the difference was 5.5%, and the difference dropped rapidly to $< 1\%$ for $A > 3t$ (for a plot, see Supplementary Information). This is a remarkably good match, within the 1-3% error of the FEM simulations. The experimental results followed the same trend but were once again systematically lower by 10%.

The axial stiffness falls rapidly with increasing A . For a metal film 1000 \AA thick, a crenellation height of 1 \mu m ($A = 10t$) reduces the stiffness by three orders of magnitude compared to $A = t$, and for crenellation height of 2.5 \mu m , four orders of magnitude. These amplitudes are readily achievable with standard microfabrication approaches, both inplane (by photolithographic patterning) and out-of-plane (by etching, molding).

Figure 7b gives the fraction of axial beam displacement due to the bending of the horizontal and vertical segments. For small A , the dominant contribution to the lowering of the stiffness comes from the bending of the horizontal

segment (Figure 7b), which has a length of 25 μm (Figure 1a). The bending of the vertical segment becomes more significant when $A = 75t$ ($= 0.75\lambda = 3H$), as expected from Equation (21).

3.4.2 Bending Stiffness

According to the analytical model, the bending stiffness of the rectangle is (Supplementary Information for the derivation):

$$(22) \quad \frac{k_y}{Ew} = \frac{3t^3}{2(6L^3 + 73AL^2)}$$

This expression has a linear dependence on $1/A$, whereas the axial stiffness depends on $1/A^3$, accounting for the much smaller effect of crenellation. The bending stiffness drops by less than 50% for a crenellation amplitude of 10, compared to a factor of greater than 1000 for the axial stiffness.

Figure 8a shows the bending stiffness from the analytical model, FEM simulations, and experiments. Differences between the FEM simulations and the analytical estimate are less than 2.7% (for a plot of the differences, see Supplementary Information). The experimental values follow the same trend, but with the usual offset.

The relative contributions to the deflection from the horizontal and vertical segments are shown in Figure 8b. Again, as expected, for small A the dominant contribution to the lowering of the stiffness comes from the bending of the horizontal segments. From Equation (22), the vertical segments become of equal importance when $A = Lt/12 = 300t/12 = 25t$. Thereafter, the moments acting on the vertical segments become more significant.

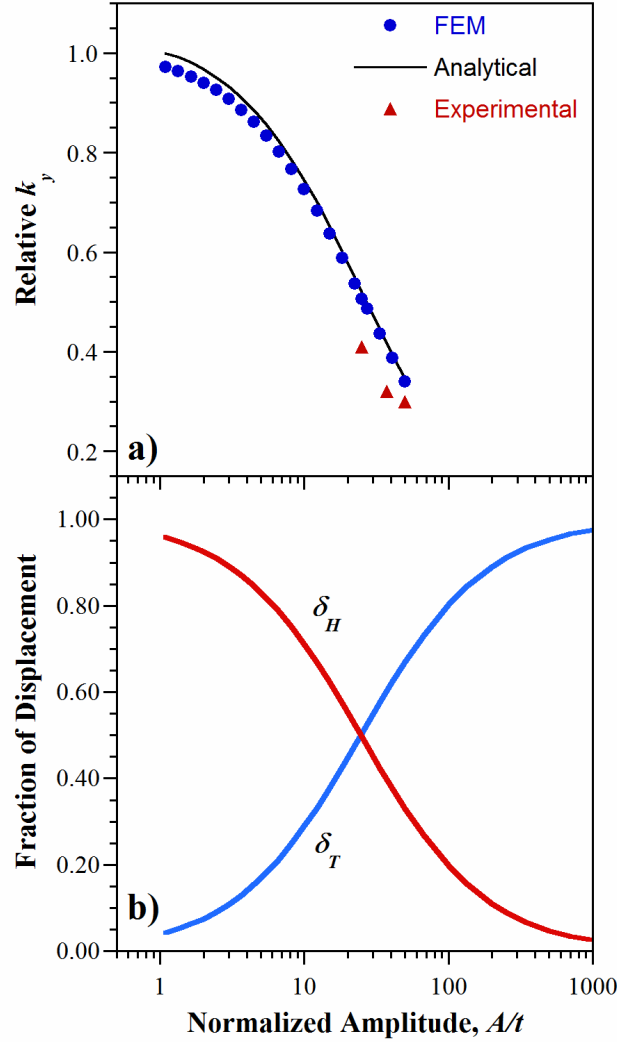
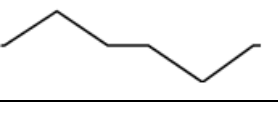
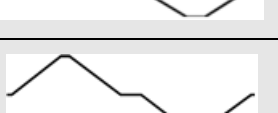
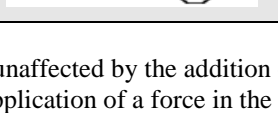


Figure 8. a) Bending stiffness (simulation, analytical estimation, and experimental) relative to that of a straight beam as a function of crenellation amplitude. b) The fraction of bending displacement due to bending of the horizontal (δ_H) and vertical (δ_T) segments, given by the analytical approach.

3.5 Straight Regions at the Horizontal Center of Symmetry

Straight horizontal sections placed at the vertical center of the structure do not bend upon the application of a force in the x -direction, and so were not expected to contribute to lowering the axial stiffness. To confirm this hypothesis, FEM simulations were performed on triangular beams ($\alpha = 45^\circ$, $A = 25t$, one period length, $2 \mu\text{m}$ long end-attachments) upon changes in the lengths and positions of additional horizontal segments. The structures therefore differed in length. Table 2 shows the results.

Table 2. Axial and bending stiffness found by FEM for a triangular beam with added straight regions of varying length and vertical position, normalized by the triangular shape.

Straight Regions, Length	Straight Region, Locations	Length	Schematic	Relative Axial Stiffness	Relative Bending Stiffness
0	–	100		1.00	1.00
20	center	120		1.02	0.62
10	both ends	120		1.00	0.63
10, 5	center, both ends	120		1.02	0.63
5	peaks	110		0.81	0.77
10	peaks	120		0.69	0.62
5, 10	peaks, center	120		0.82	0.62

As expected, the axial stiffness is essentially unaffected by the addition of straight sections at the vertical center of symmetry (since they do not bend upon the application of a force in the x -direction), either in the middle of the beam or at the ends. The addition of small straight sections off the vertical center, however, lowers the stiffness, as was also seen in Figure 4. The off-center sections bend and thus contribute to increase overall deflection.

As shown above, the bending stiffness is proportional to the total length of the structure. This remains true upon the addition of horizontal segments anywhere, which serve to increase the length: the bending stiffness again decreases linearly with total length.

3.6 Elastomer under a Crenellated Beam

Metal out-of-plane crenellations and inplane meanders have been used to form compliant electrodes on elastomeric substrates. To fabricate the former, a metal film can be deposited onto an elastomer having a corrugated surface, as demonstrated by Benslimane and Gravesen [16] and subsequently patented and used by Danfoss PolyPower A/S in their commercial DEA material [24]. The corrugation can be formed by techniques such as molding or etching, producing angled corners. Alternatively, the metal can be deposited onto a stretched elastomer, spontaneously forming smooth sinusoid-like wrinkles when the elastomer is relaxed [17]. To form inplane meanders, a metal film can be deposited onto a flat elastomer substrate and patterned photolithographically into a meander line. Extensive modeling and experimental work has been done on the inplane meanders [5,9,11-13,25-32], so it will not be discussed here.

An elastomer with one rectangular crenellated surface coated by an electrode (Figure 9) was modeled by FEM to find the structure's axial and bending stiffness. The thickness $t_{elast.}$ is the thickness of the elastomer underneath the crenellated part, from the flat bottom surface of the elastomer to the trough of the crenellated electrode. The amplitude $2A$, electrode thickness t , structure length L , and period λ are defined the same way as above.

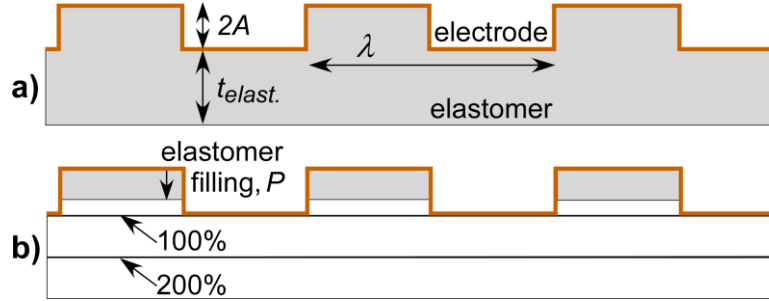


Figure 9. Schematic of an elastomer with a crenellated, electrode-covered top surface and a flat uncoated bottom surface. (a) In one set of FEM simulations, $2A$ was varied and the other dimensions were kept fixed at $t_{elast.} = 50 \mu\text{m}$, $\lambda = 100 \mu\text{m}$, $L = 305 \mu\text{m}$, $t = 1 \mu\text{m}$. (b) In a second set of simulations, the percentage of elastomer filling was increased with the electrode dimensions fixed. The lines show the levels at which 100% and 200% of the crenellation are filled.

The effect on stiffness from filling the crenellated shape with an elastomer is shown in Figure 10. The filling percentage P is measured from the top of the electrode and given as a fraction of $2A$: at 100% the crenellation is completely filled (Figure 9b). In these simulations, the Poisson's ratio, ν for the electrode was 0.34, which is a typical value for a metal [22], and for the elastomer it was $\nu = 0.49$, the value for PDMS [33].

The axial stiffness k_{fx} of the filled structure is sigmoidal with P (Figure 10a), showing little change up to 50% filling. Above 50%, k_{fx} increases quasi-linearly with P until 200%, and then it flattens out to approximately twice the unfilled stiffness. The axial stiffness of the filled structure is thus dominated by the electrode stiffness, as is confirmed below.

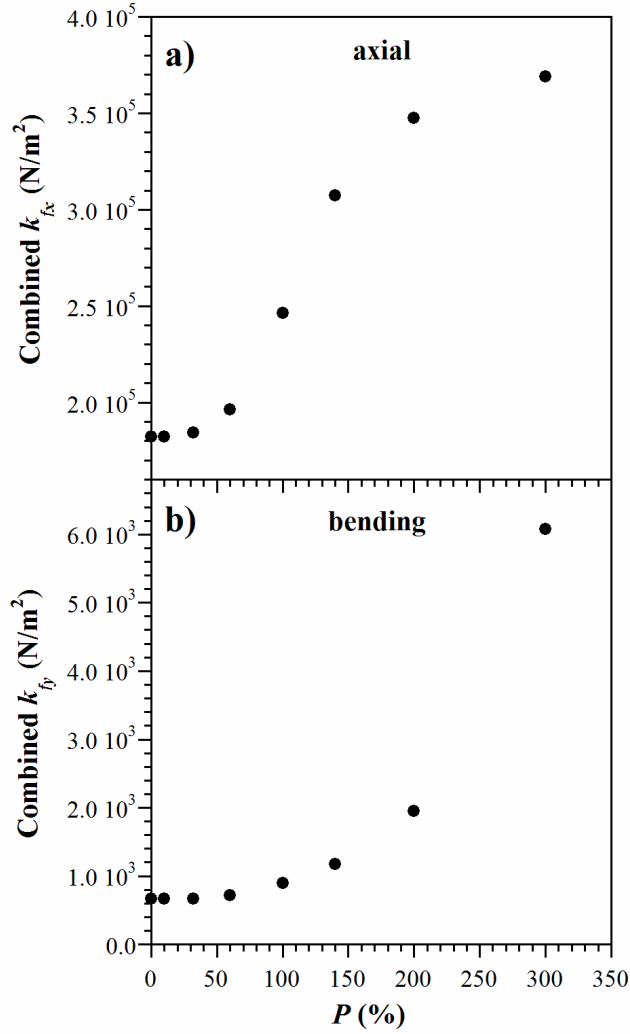


Figure 10. The (a) axial and (b) bending stiffness of a rectangular crenellated beam as a function of elastomer filling amount ($t = 1 \mu\text{m}$, $2A = 25 \mu\text{m}$, $E_{\text{electrode}} = 120 \text{ GPa}$, and $E_{\text{elastomer}} = 10^{-3} \text{ GPa}$).

The bending stiffness k_y follows an x^3 relationship with thickness added to the original structure (Figure 10b). Thus, filling to 100% does not significantly change the bending stiffness, but thereafter the stiffness increases as P^3 . (Thicknesses greater than 300% were not explored in our study). Unlike for the axial case, the bending stiffness becomes dominated by the elastomer.

To gain insight into the shape of the curves in Figure 10, the electrode modulus $E_{\text{electrode}}$ was varied between 5 and 120 GPa while keeping the elastomer modulus $E_{\text{elastomer}}$ constant at 10^{-3} GPa. Six different crenellation amplitudes were studied between $2A = 2 \mu\text{m}$ and $200 \mu\text{m}$ for a metal film thickness of $t = 1 \mu\text{m}$. The crenellated area was in all the combined cases completely filled, and under the crenellation was an elastomer of thickness $t_{\text{elast.}} = 50 \mu\text{m}$ (as illustrated in Figure 9a). The stiffness is plotted versus the ratio of the moduli $E_{\text{electrode}}/E_{\text{elastomer}}$ and versus the crenellation height ($2A$) in Figure 11. Crenellated electrodes alone are shown for comparison, and for these $E_{\text{electrode}}$ was divided by the 10^{-3} GPa modulus of elastomer. The crenellated elastomer alone is also included (as for the combined structure, $50 \mu\text{m}$ of elastomer plus a $2A$ crenellation height above that), $E_{\text{electrode}} = 0$. This is therefore drawn as a horizontal line for visualization. (The elastomer stiffnesses for the different $2A$ overlap and so cannot be distinguished.) Adding the $2A = 25 \mu\text{m}$ crenellated electrode (open black triangles) and the $2A = 25 \mu\text{m}$ elastomer (horizontal gray line) yields the dashed gray line. The axial stiffness of the straight beam ($2A = 0$) with underlying elastomer thickness $50 \mu\text{m}$ is too large to be included in Figure 11a (it is 4 orders of magnitude greater than the

crenellated structures, as presented in Table 1), but the bending stiffness of the straight beam is shown as the red line in Figure 11b. (The k_{fy} for $2A = 2 \mu\text{m}$ and $6 \mu\text{m}$ are also much larger and lie beyond the scale of Figure 11c.)

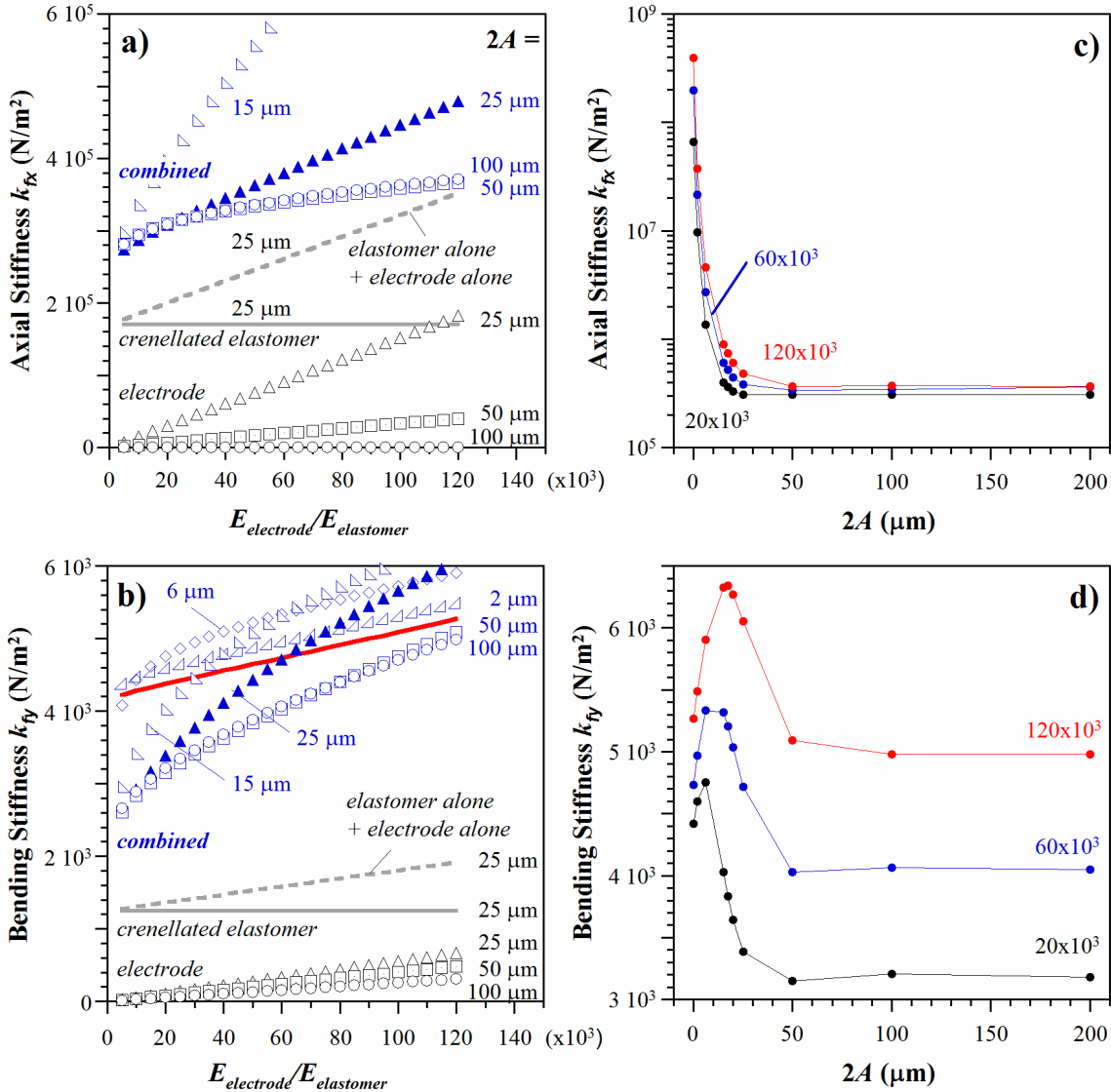


Figure 11. a) Axial and b) bending stiffness of the combined elastomer + metal structure shown in Figure 9 as a function of the electrode:elastomer stiffness ratio for different crenellation amplitudes $2A$ and a $50 \mu\text{m}$ thickness of elastomer under the crenellation (blue symbols, top). Filled triangles indicate the structure of Figure 10 with $P = 200\%$. Also shown are the stiffnesses of the crenellated electrodes alone (black symbols, bottom), the crenellated elastomer alone ($50 \mu\text{m} + 2A$, solid gray line), and the sum of these two (dashed gray line). The red line in (b) shows the bending stiffness of a $50 \mu\text{m}$ thick layer of PDMS with an overlying flat metal film ($2A = 0$). c) Axial and d) bending stiffness of the structure as a function of $2A$ for three values of $E_{electrode}/E_{elastomer}$ (solid lines are guides to the eye).

Looking at the axial stiffness of the combined structures (blue symbols) in Figure 11a, the axial stiffness increases with $E_{electrode}/E_{elastomer}$ for all values of $2A$, as expected. Also, the expected lowering of stiffness with crenellation height is seen, just as for the electrode alone (black symbols). One might, however, have assumed that the combined axial stiffness k_{fx} would be close to that found by the simple addition of the individual electrode and crenellated elastomer stiffnesses, but that is not the case. Comparing the $25 \mu\text{m}$ combined structure (solid blue triangles) with the sum (dashed line) of the electrode alone (open triangles) and the elastomer alone (solid line), the combined structure is offset upward by a constant 10^5 N/m^2 . The interaction between the electrode and the elastomer arising from bonding the two constrains the axial motion, raising k_{fx} . Another thing to note in Figure 11a is that when $2A$ is

large, unlike for the electrode alone, the combined structure's axial stiffness increases sublinearly with the modulus of the electrode.

Figure 11c shows the dependence of k_{fx} on $2A$ for two values of the relative electrode stiffness. (The range of values in Figure 11a is indicated to allow comparison of the two plots.) There are two distinct regimes of behavior: (1) electrode stiffness dominated and (2) elastomer stiffness dominated. The initial slope at small $2A$ is consistent with the results of Figure 7, where the axial stiffness of the crenellated electrode decreases as $1/A^3$; for illustration, the red line in Figure 11c decreases as $1/A^3$. For larger $2A$, above $50\ \mu\text{m}$, the stiffness approaches that of the crenellated elastomer alone, shown by the gray line. This plot illuminates the curves in Figure 11a: for $2A < 50\ \mu\text{m}$, where the crenellated electrode dominates, there is a linear relationship between k_{fx} and $E_{\text{electrode}}/E_{\text{elastomer}}$. For $2A \geq 50$, where the elastomer dominates, there is a nonlinear relationship between k_{fx} and $E_{\text{electrode}}/E_{\text{elastomer}}$ because k_{fx} approaches a constant value.

Figure 11b shows the variation of bending stiffness k_{fy} with $E_{\text{electrode}}/E_{\text{elastomer}}$. As in the case of the axial stiffness, k_{fy} is not a simple addition of the individual electrode and crenellated elastomer stiffnesses. Furthermore, the combined structure is in some cases stiffer than the straight beam (red line), and in other cases less stiff. Looking first at the smallest corrugation, $2A = 2\ \mu\text{m}$, the stiffness is close to that for the uncrenellated beam, being offset slightly upward. This is as expected. For $2A = 6\ \mu\text{m}$, the slope is greater, but for the smallest $E_{\text{electrode}}/E_{\text{elastomer}}$ values, the structure is actually less stiff than the straight beam. This curve, and the later ones, are also nonlinear. This trend continues for $2A = 15\ \mu\text{m}$, which is almost half as stiff as the straight beam for small $E_{\text{electrode}}/E_{\text{elastomer}}$, equally stiff at $E_{\text{electrode}}/E_{\text{elastomer}} = 30 \times 10^3$, and thereafter increasing even more strongly with $E_{\text{electrode}}/E_{\text{elastomer}}$ than $2A = 6\ \mu\text{m}$ did. For larger values of $2A$, the curves all have the same stiffness at small $E_{\text{electrode}}/E_{\text{elastomer}}$. However, the slopes reverse trend and become less steep with increasing $2A$. In fact, with further increases in crenellation amplitude, the stiffness decreases.

Showing the data as a function of $2A$ in Figure 11d for three values of $E_{\text{electrode}}/E_{\text{elastomer}}$ again helps to explain the behavior. At $2A = 0$ the beam is uncrenellated. Unlike for axial stiffness, adding a small crenellation actually initially *increases* the bending stiffness k_{fy} . It reaches a peak at $2A \approx 15\ \mu\text{m}$, then decreases and levels off above $2A \approx 50\ \mu\text{m}$ to a value that is lower than that of the flat beam. (The $2A = 50\ \mu\text{m}$ point with $t_{\text{elast.}} = 50\ \mu\text{m}$ corresponds to $P = 200\%$ in Figure 10.) Like in Figure 11c, for large crenellations the stiffness becomes independent of $2A$. Increasing values of $E_{\text{electrode}}/E_{\text{elastomer}}$ result in an overall upshift in stiffness as well as a shift in peak position to higher values of $2A$. These results mean that for bending structures, both $2A$ and $E_{\text{electrode}}/E_{\text{elastomer}}$ must be chosen to ensure the desired behavior, with both lesser and greater stiffness than a straight beam possible, depending on the parameters. A bending dielectric elastomer actuator with one straight electrode and one crenellated electrode could bend either toward or away from the straight side by changing the design. It should be noted, however, that changes in bending stiffness with crenellation are relatively small (the y-axis is linear) compared with changes in the axial stiffness (for which the y-axis has a log scale).

4 Discussion and Conclusions

We have presented design guidelines based on analytic models derived from beam theory for using out-of-plane crenellation or inplane meandering to reduce the stiffness of a beam. We have derived relatively simple analytical expressions that can be readily applied and that accurately predict the axial and bending stiffness.

The effect of crenellation on axial stiffness is substantially larger than it is on bending stiffness. For both, decreasing the beam thickness and increasing the angle of the vertical-going segments lowers stiffness. Increasing α affects axial stiffness primarily by increasing the length of the off-midline horizontal segments, while it affects bending stiffness primarily by increasing the total length of the beam. However, the most effective way to reduce the axial stiffness is by increasing the height of the crenellations, which can lower it by orders of magnitude.

Curved meanders are preferred over those with sharp corners because the latter experience larger stress concentrations that can lead to premature failure upon repeated extension. However, from a microfabrication point of view, out-of-plane sinusoidal curves are more challenging to fabricate than trapezoidal structures. (One can produce any desired shape inplane by creation of an appropriate mask.) Instead, one can readily produce out-of-plane rectangular crenellation by anisotropic dry etching of the substrate, trapezoidal crenellation with $\alpha = 54.7^\circ$ by Si anisotropic wet etching, and partially curved structures by isotropic wet etching. With other fabrication methods, corrugated shapes are produced by bending or folding sheets, strips, or wires, and weaving results in sinusoidal-like corrugation.

When fabricating axial devices, appropriated space for extension must be provided. Thus, it is important to note that axial tension in the x -direction leads not only to displacement in the x -direction, but also to displacement in the y -direction because of out-of-plane deformation of the crenellated shapes [34]. For a $1\ \mu\text{m}$ prescribed displacement in x , a more than $1\ \mu\text{m}$ displacement occurs in y . For bending, on the other hand, displacement in the y -direction is not coupled to significant x -displacement.

Elastomer-filled, metal-film-coated structures with moderate crenellation amplitudes are a thousand times less stiff when stretched in the axial direction than uncrenellated beams, approaching the stiffness of the elastomer alone. Even a small crenellation decreases the axial stiffness dramatically. However, the situation is quite different for bending, which is weakly affected by crenellation. While for large crenellations the bending stiffness drops somewhat, at low crenellation amplitude the stiffness is actually higher than that of a straight beam. Thus, when designing crenellated bending structures, appropriate values of the electrode stiffness and crenellation height must be chosen to achieve the desired behavior.

Acknowledgements

We would like to thank Mr. Zhao Zhang for valuable discussions and guidance. We would like to thank Deepa Sritharan for independently duplicating some of the experiments. The material in this paper is based on work supported by the National Science Foundation under grant no. CNS 0931878.

Supplementary Material

The supplementary information includes information about the COMSOL simulation, model validation, and experimental data. In addition, the axial stiffness derivation and the simplification of bending stiffness to rectangular crenellation are given. Finally, the difference between the analytical and FEM for various amplitudes of rectangular crenellation is also illustrated.

5 References

1. G. K. Fedder, "Simulation of Microelectromechanical Systems," Electrical Engineering and Computer Sciences, University of California at Berkeley, Berkeley (1994).
2. P. A. Manoharan and D. Nedumaran, "Modeling-Simulation and analysis of MEMS capacitive millibar pressure sensor," *J. Nanotechnol. Eng. Med.*, 1, 041003-041001 (2010).
3. M. Lishchynska, C. O'Mahony, O. Slattery, and R. Behan, "Comprehensive spring constant modelling of tethered micromechanical plates," *J. Micromech. Microeng.*, 16 (6), S61-S67 (2006).
4. Y. L. Loo, T. Someya, K. W. Baldwin, Z. N. Bao, P. Ho, A. Dodabalapur, H. E. Katz, and J. A. Rogers, "Soft, conformable electrical contacts for organic semiconductors: High-resolution plastic circuits by lamination," *Proc. Natl. Acad. Sci. U. S. A.*, 99 (16), 10252-10256 (2002).
5. S. P. Lacour, J. Jones, S. Wagner, T. Li, and Z. G. Suo, "Stretchable interconnects for elastic electronic surfaces," *Proc. IEEE*, 93 (8), 1459-1467 (2005).
6. N. Tiercelin, P. Coquet, R. Sauleau, V. Senez, and H. Fujita, "Polydimethylsiloxane membranes for millimeter-wave planar ultra flexible antennas," *J. Micromech. Microeng.*, 16 (11), 2389-2395 (2006).
7. R. Pelrine, R. Kornbluh, J. Joseph, R. Heydt, Q. B. Pei, and S. Chiba, "High-field deformation of elastomeric dielectrics for actuators," *Mater. Sci. Eng. C-Biomimetic Supramol. Syst.*, 11 (2), 89-100 (2000).
8. D. W. Pashley, "A study of the deformation and fracture of single-crystal gold films of high strength inside an electron microscope," *Proc. R. Soc. Lond. A*, 255 (1281), 218-231 (1960).
9. T. Li, Z. Y. Huang, Z. Suo, S. P. Lacour, and S. Wagner, "Stretchability of thin metal films on elastomer substrates," *Appl. Phys. Lett.*, 85 (16), 3435-3437 (2004).
10. R. Kornbluh, R. Pelrine, J. Joseph, R. Heydt, Q. Pei, and S. Chiba, "High-field electrostriction of elastomeric polymer dielectrics for actuation," *Smart Structures and Materials 1999: Electroactive Polymer Actuators and Devices*, Newport Beach, CA, USA, (SPIE), vol. 3669, edited by Y. Bar-Cohen, p. 149-161 (1999).
11. D. Gray, J. Tien, and C. Chen, "High-conductivity elastomeric electronics," *Adv. Mater.*, 16 (5), 393-397 (2004).
12. T. Li, Z. G. Suo, S. P. Lacour, and S. Wagner, "Compliant thin film patterns of stiff materials as platforms for stretchable electronics," *J. Mater. Res.*, 20 (12), 3274-3277 (2005).
13. D. Brosteaux, F. Axisa, M. Gonzalez, and J. Vanfleteren, "Design and fabrication of elastic interconnections for stretchable electronic circuits," *IEEE Electron Device Lett.*, 28 (7), 552-554 (2007).
14. S. Wagner, S. P. Lacour, J. Jones, P. H. I. Hsu, J. C. Sturm, T. Li, and Z. G. Suo, "Electronic skin: architecture and components," *Physica E*, 25 (2-3), 326-334 (2004).
15. C. Liu, Foundations of MEMS, (Pearson Education Inc., Upper Saddle River, New Jersey, 2006).
16. M. Benslimane, P. Gravesen, and P. Sommer-Larsen, "Mechanical properties of dielectric elastomer actuators with smart metallic compliant electrodes," *Smart Structures and Materials 2002: Electroactive*

- Polymer Actuators and Devices (EAPAD), San Diego, CA, USA (SPIE), vol. 4695, edited by Y. Bar-Cohen, p. 150-157 (2002).
17. N. Bowden, S. Brittain, A. G. Evans, J. W. Hutchinson, and G. M. Whitesides, "Spontaneous formation of ordered structures in thin films of metals supported on an elastomeric polymer," *Nature*, 393 (6681), 146-149 (1998).
 18. A. Dec and K. Suyama, "Micromachined electro-mechanically tunable capacitors and their applications to RF IC's," *IEEE Trans. Microw. Theory Tech.*, 46 (12), 2587-2596 (1998).
 19. M. Bails, J. A. Martinez, S. P. Levitan, I. Avdeev, M. Lovell, and D. M. Chiarulli, "Computational prototyping of an RF MEMS switch using chatoyant," *Nanotech 2004*, Boston, MA, vol. 2 (2004).
 20. M. Lishchynska, N. Cordero, and O. Slattery, "Development of behavioural models for mechanically loaded microcantilevers and beams," *Analog Integr. Circuits Process.*, 44 (2), 109-118 (2005).
 21. T. Maleki, G. Chitnis, A. Panja, and B. Ziaie, "Single-layer elastomeric out-of-plane actuator with asymmetric surface profile," *Solid-State Sensors, Actuators, and Microsystems Workshop, Hilton Head Workshop, Hilton Head, South Carolina, (Transducer Research Foundation, Inc.),* edited by D. J. M. a. K. L. Turner (June 6 - 10, 2010).
 22. Handbook on materials selection, edited by M. Kutz (John Wiley & Sons, New York, 2002).
 23. J. M. Gere and S. P. Timoshenko, Mechanics of Materials, 4th ed. (PWS Publishing Company, Boston, 1997).
 24. H.-E. Kiil and M. Y. Benslimane, "Scalable industrial manufacturing of DEAP," *Electroactive Polymer Actuators and Devices (EAPAD) 2009*, San Diego, (SPIE), edited by Y. Bar-Cohen; and T. Wallmersperger, p. 72870R (2009).
 25. S. P. Lacour, S. Wagner, Z. Y. Huang, and Z. Suo, "Stretchable gold conductors on elastomeric substrates," *Appl. Phys. Lett.*, 82 (15), 2404-2406 (2003).
 26. T. Li and Z. Suo, "Deformability of thin metal films on elastomer substrates," *Int. J. Solids Struct.*, 43 (7-8), 2351-2363 (2006).
 27. S. P. Lacour, D. Chan, S. Wagner, T. Li, and Z. G. Suo, "Mechanisms of reversible stretchability of thin metal films on elastomeric substrates," *Appl. Phys. Lett.*, 88 (20), 3 (2006).
 28. S. P. Lacour, J. Jones, Z. Suo, and S. Wagner, "Design and performance of thin metal film interconnects for skin-like electronic circuits," *IEEE Electron Device Lett.*, 25 (4), 179-181 (2004).
 29. S. P. Lacour, S. Wagner, R. J. Narayan, T. Li, and Z. G. Suo, "Stiff subcircuit islands of diamondlike carbon for stretchable electronics," *J. Appl. Phys.*, 100 (1), 6 (2006).
 30. S. P. Lacour, S. Wagner, H. Prahlad, and R. Pelrine, "High voltage photoconductive switches of amorphous silicon for electroactive polymer actuators," *J. Non-Cryst. Solids* 736-739 (2004).
 31. T. Li, Z. Y. Huang, Z. C. Xi, S. P. Lacour, S. Wagner, and Z. Suo, "Delocalizing strain in a thin metal film on a polymer substrate," *Mech. Mater.*, 37 (2-3), 261-273 (2005).
 32. T. Li and Z. Suo, "Ductility of thin metal films on polymer substrates modulated by interfacial adhesion," *Int. J. Solids Struct.*, 1696-1705 (2007).
 33. C. Kluge, N. Galler, H. Dittbacher, and M. Gerken, "Modeling of electrically actuated elastomer structures for electro-optical modulation," *Appl. Phys. A-Mater. Sci. Process.*, 102 (2), 407-413 (2011).

34. W. C. Young, Roark's Formula for Stress & Strain, 6th ed. (McGraw-Hill Inc, 1989).

Supplementary Information
for
**Design of Compliant Meanders for Applications in
MEMS, Actuators, and Flexible Electronics**

Bavani Balakrisnan, Aleksandar Nacev, Jeffery M. Burke, Abhijit Dasgupta, and
Elisabeth Smela

University of Maryland, College Park, Maryland 20742

SI-1. Simulation: Implementation and Computational Parameters

Governing Equations

The software package COMSOL Multiphysics (version 3.5a) was used for implementing the numerical simulations. COMSOL solved the following discretized structural mechanics partial differential equation (PDE):

$$(SI-1) \quad \vec{F} = -\nabla \cdot \sigma,$$

where F is the force vector and ∇ is the differential operator [1]. The stress tensor σ was classically defined as:

$$(SI-2) \quad \sigma = \begin{bmatrix} \sigma_x & \tau_{xy} & \tau_{xz} \\ \tau_{yx} & \sigma_y & \tau_{yz} \\ \tau_{zx} & \tau_{zy} & \sigma_z \end{bmatrix}, \quad \tau_{xy} = \tau_{yx}, \quad \tau_{xz} = \tau_{zx}, \quad \tau_{yz} = \tau_{zy},$$

where σ_x , σ_y , and σ_z are the normal stresses acting in the x , y , and z directions, respectively, and τ_{xy} , τ_{xz} , and τ_{yz} are the shear stresses. The notation τ_{xy} denotes that the shear stress acts on face x in the y -direction. Similarly, the classical strain tensor [2] was defined as:

$$(SI-3) \quad \varepsilon = \begin{bmatrix} \varepsilon_x & \varepsilon_{xy} & \varepsilon_{xz} \\ \varepsilon_{xy} & \varepsilon_y & \varepsilon_{yz} \\ \varepsilon_{xz} & \varepsilon_{yz} & \varepsilon_z \end{bmatrix},$$

where

$$(SI-4) \quad \begin{aligned} \varepsilon_x &= \frac{\partial u}{\partial x} & \varepsilon_{xy} &= \frac{\gamma_{xy}}{2} = \frac{1}{2} \left(\frac{\partial u}{\partial y} + \frac{\partial v}{\partial x} \right) \\ \varepsilon_y &= \frac{\partial v}{\partial y} & \varepsilon_{yz} &= \frac{\gamma_{yz}}{2} = \frac{1}{2} \left(\frac{\partial v}{\partial z} + \frac{\partial w}{\partial y} \right) \\ \varepsilon_z &= \frac{\partial w}{\partial z} & \varepsilon_{xz} &= \frac{\gamma_{xz}}{2} = \frac{1}{2} \left(\frac{\partial u}{\partial z} + \frac{\partial w}{\partial x} \right) \end{aligned}$$

with u , v , and w defined as the displacements in the x , y and z directions, respectively, ε_x , ε_y , and ε_z as the normal strains, and γ_{xy} , γ_{yz} , and γ_{xz} as the shear strains.

Using classical structural mechanics, the relationship between the strain and stress tensors is obtained by reorganizing the strain and stress tensors into a six-element vector form, which simplifies the numerical simulation. The relationship between the stress and strain vectors is

$$(SI-5) \quad \sigma = D \varepsilon,$$

where D is the elasticity matrix. By observing that three elements in the stress tensor are equivalent to three others (see equation (SI-2)), one can write

$$(SI-6) \quad \sigma = \begin{bmatrix} \sigma_x \\ \sigma_y \\ \sigma_z \\ \tau_{xy} \\ \tau_{yz} \\ \tau_{xz} \end{bmatrix}, \quad \varepsilon = \begin{bmatrix} \varepsilon_x \\ \varepsilon_y \\ \varepsilon_z \\ \gamma_{xy} \\ \gamma_{yz} \\ \gamma_{xz} \end{bmatrix}.$$

The elasticity matrix is then a 6 x 6 matrix defined as:

$$(SI-7) \quad D = \frac{E}{(1+\nu)(1-2\nu)} \begin{bmatrix} 1-\nu & \nu & \nu & 0 & 0 & 0 \\ \nu & 1-\nu & \nu & 0 & 0 & 0 \\ \nu & \nu & 1-\nu & 0 & 0 & 0 \\ 0 & 0 & 0 & \frac{1-2\nu}{2} & 0 & 0 \\ 0 & 0 & 0 & 0 & \frac{1-2\nu}{2} & 0 \\ 0 & 0 & 0 & 0 & 0 & \frac{1-2\nu}{2} \end{bmatrix},$$

where E is the Young's modulus and ν is Poisson's ratio. The above equations can be solved to give the displacement (or strain shown in equation (SI-5)) of an object from the induced stresses (calculated from the applied forces in equation (SI-1)) and the material properties described by the displacement matrix (equation (SI-7)).

Boundary Conditions and Constraints

Discretization involves breaking the geometry into small volume elements (mesh elements). The stresses, strains, and resultant deflections are calculated for each element based on its mechanical properties (in this case, the Young's modulus and Poisson ratio) and the specified boundary conditions.

The simulation was two-dimensional (2D), meaning that it looked at the cantilever cross section and did not consider changes in the width direction (z direction). This saved computation time without loss of accuracy. To simplify to two dimensions, the third dimension was accounted for by specifying that it held no stress (σ_z , τ_{xz} , and τ_{yz} are zero). This assumption is reasonable for structures whose out-of-plane width is much greater than their length. Agreement between the full 3D and the 2D model was checked for the case rectangular crenellation with $A = 25$; results were within 7%.

The boundary conditions for the 2D model are summarized in SI_Table 1, completing the definition of the model. The reaction forces acting upon the entire structure are determined by solving the model. The structure's reaction forces are computed by integrating over the right-hand boundary (determined using equation (SI-1)) subject to the requirement that the sum of all forces acting upon a structure is zero.

SI_Table 1. Boundary conditions used in the simulations.

Boundary	Physical Interpretation	Definition
Left hand boundary	No horizontal or vertical movement.	$u = 0, v = 0$
Right hand boundary	Prescribed physical displacement	$u = u_{prescribed}$ OR $v = v_{prescribed}$
All other boundaries	Continuity	Solved by Equations (SI-1) - (SI-7)

Meshing

With any finite element modeling (FEM), the mesh size must be sufficiently small to capture the physics, including any steep gradients in the solutions that might occur at edges, corners, and interfaces. Mesh refinement, a technique in which the mesh element size is systematically reduced, was enacted until the solution converged to a stable value (a variation of $\leq 1\%$); in most instances 2 to 3 mesh refinements were sufficient. The shape of the mesh is also a consideration. We used a free (not fixed or uniformly sized) triangular (not quad) mesh because it ensured that the physics were accurately captured for any geometry: curves can be modeled more accurately using triangular meshes compared to square or quad meshes [1].

Solving

The COMSOL solver UMFPAK, an unsymmetric multifrontal method designed to solve asymmetric sparse linear systems [3], was used to solve the system of equations, and it was sufficient to generate a converged solution. Issues with convergence arose when the model was displaced by large values (on the order of the length of the model, $A = 100$); this problem was resolved by fixing the structure at a single point instead of along a boundary.

Post-Processing

In order to obtain accurate values for the reaction force under a prescribed displacement, the displacement in the perpendicular direction must be free to change, meaning that the right-hand boundary only contains a prescribed physical displacement in the x -direction (or y -direction) for axial (bending) stiffness. This ensures that the force exerted upon the structure is in only a single direction while allowing the structure to freely deform, and thereby to compensate for that geometric change. As mentioned previously, the model's reaction forces due to the prescribed displacement are determined by integrating the reaction forces (equation (SI-1) from the solved model) at the right hand boundary.

SI-2. Model Validation with Cantilevered Rectangular Beam

The axial stiffness of a rectangular cantilevered beam is given by [2],

$$(SI-8) \quad k_x = \frac{Ewt}{L},$$

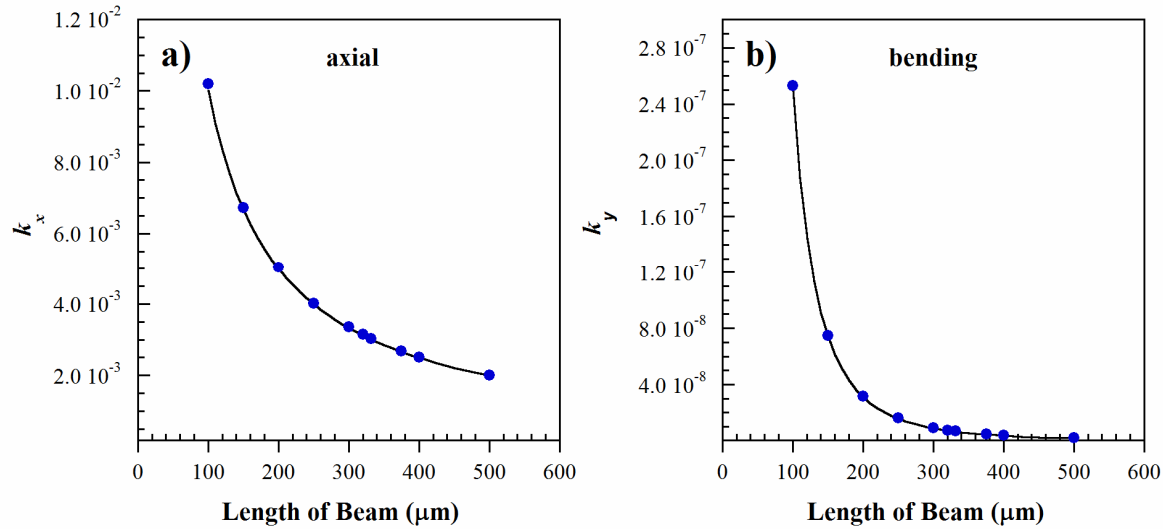
and its bending stiffness is given by

$$(SI-9) \quad k_y = \frac{Ewt^3}{4L^3},$$

where E is the Young's modulus, w is the width of the beam, t is its thickness, and L is its length.

As a control to check that the COMSOL simulations were working properly, the stiffness of a straight cantilevered beam was found. The beam was $1 \mu\text{m}$ thick and had a length L varying from 100 to $500 \mu\text{m}$. Since this was a 2D simulation, the width w was set to be essentially infinite so that the stress in the width direction could be considered zero; in practice this was done by setting $w = 1 \text{ m}$. A displacement of $1 \mu\text{m}$ in the $+x$ direction (along the long axis of the beam) was prescribed, and the x -direction reaction force was determined. This strain was small compared to the length and smaller than the plastic strain limit of the material. The axial stiffness was determined by dividing the reaction force by the displacement: $k_x = F_x/x$.

Similarly, to determine the bending stiffness a $1 \mu\text{m}$ displacement was applied perpendicular to the tip of the cantilever, and the y -direction reaction force was determined: $k_y = F_y/y$. As described above, it was necessary to *not* set the displacement in the other direction equal to zero.



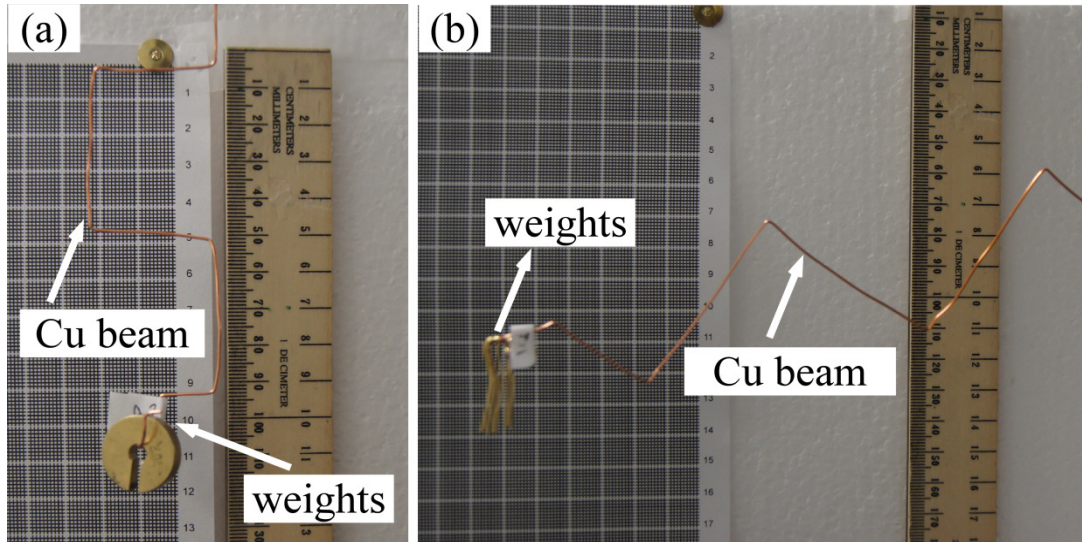
SI_Figure 1. Stiffness versus cantilever length. The blue symbols are the FEM results while the black lines are the analytical solutions using Equations (SI-8) and (SI-9) for (a) axial stiffness and (b) bending stiffness.

There was close agreement between the FEM and analytical results for both axial (SI_Figure 1a) and bending (SI_Figure 1b) stiffness. This validates the correct implementation of the FEM and allows us to proceed with some confidence to modeling more complicated structures.

SI-3. Experimental Data

SI_Figure 2 shows the experimental configuration that was used to measure axial and bending stiffnesses. Copper (Cu) wire of 0.8 mm diameter was bent into one of the simulated shapes and fixed at one end with a clamp. There were 3 periods, and each period was 8 cm long.

To measure the axial stiffness, the Cu beam was placed vertically and increasing loads between 5 and 45 g were applied at the bottom (SI_Figure 2a). For bending tests, the Cu beam was placed horizontally and increasing loads were applied at the tip (SI_Figure 2b). A printed grid with line spacings of 1 mm was placed behind the wire cantilever to allow measurement of the displacement. Close-up images of the tip of the beam were recorded using a digital camera (Sony SLT-A33), from which the deflections were obtained. Readings were taken to the nearest 1 mm. The slope of the load-deflection curve gave the stiffness. Between measurements, the position of the beam tip was measured to ensure that there had been no permanent deformation.



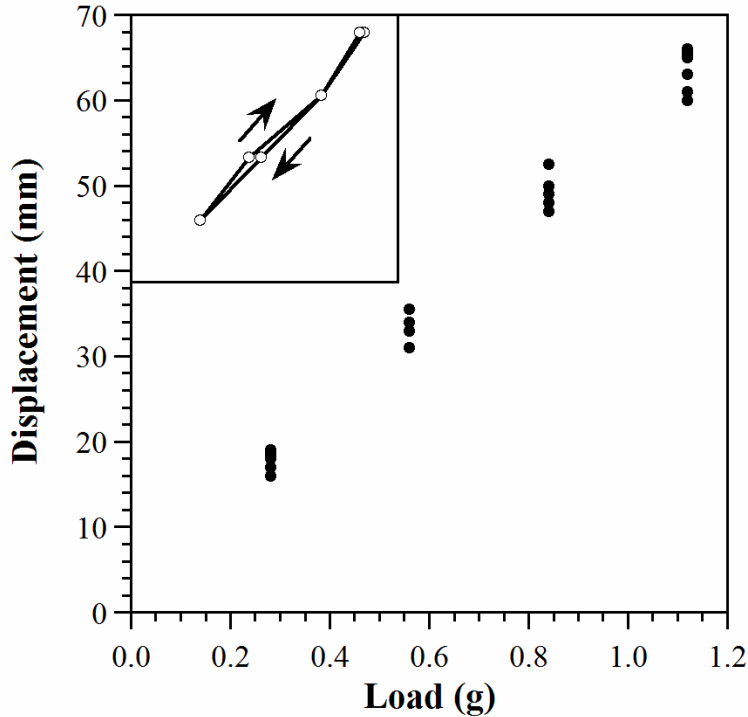
SI_Figure 2. Configuration for the experimental measurement of (a) axial and (b) bending stiffness. The ruler shows the scale.

SI_Table 2 shows the measured displacement for the five shapes and the plain beam. Four nominally identical shapes with rectangular crenellation ($\alpha = 90^\circ$, $A = 25$) were fabricated and tested to determine the variability due to fabrication differences. Two identical triangular beams were also tested, and a single structure was made for the other shapes. Variability due to mounting and unmounting was investigated by measuring on different days (Rect #1 and Trap (110,68)). A small mass (5 g for axial and 0.12 g or 0.28 g for bending) was applied to ensure that the structures were straight before further loads were added, and this point was treated as the zero deflection point. The structures were systematically loaded and then unloaded to confirm that there was no difference in the loading and unloading events.

SI_Table 2. Experimental displacements for loads applied axially and perpendicularly to the beams.

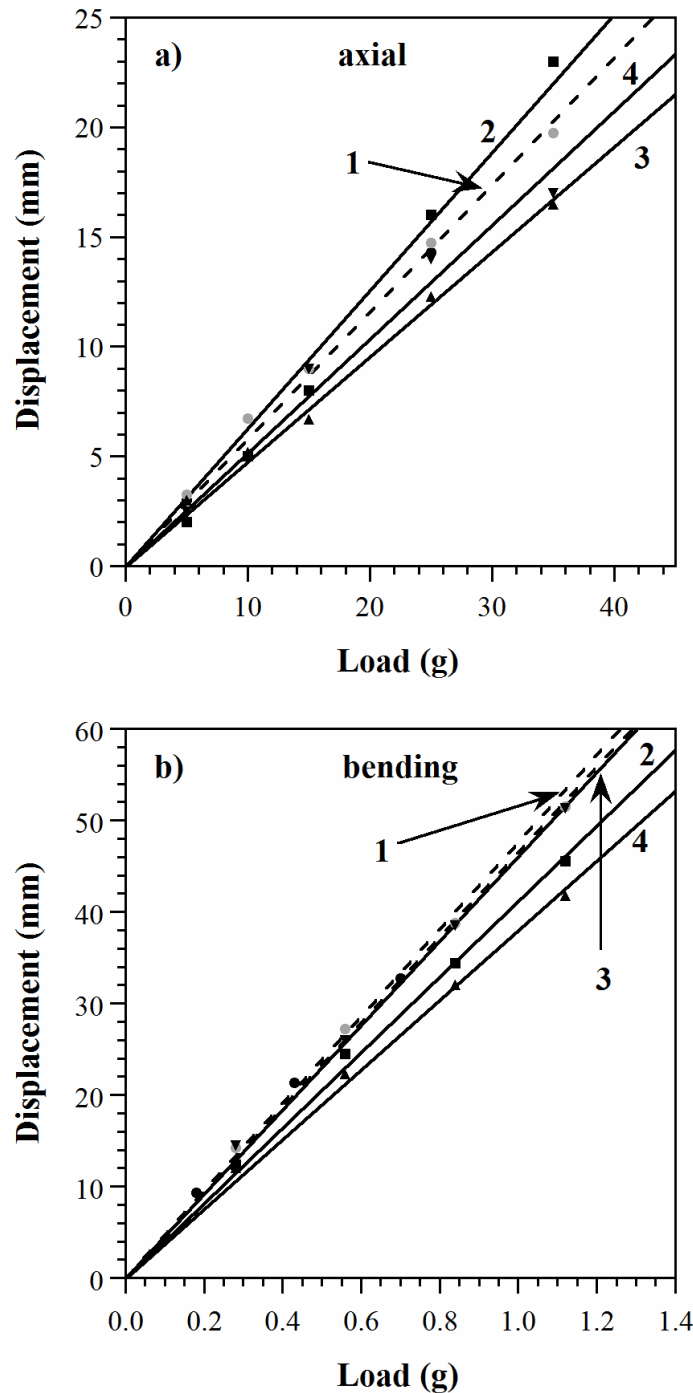
Beam	Load (g)	Axial Displacement (mm)	Load (g)	Bending Displacement (mm)
Straight Beam			0.18	3, 3, 3
			0.43	8, 8, 8
			0.70	12,12,12
Triangular (A = 25) Beam #1	5	1, 2	0.28	9, 8
	15	3, 4	0.56	17, 16
	25	5, -	0.84	25, 25
	35	7, 8	1.12	34, 32
	45	9, 10		
Triangular (A = 25) Beam #2	5	1, 2	0.28	8, 7
	15	4, 4	0.56	16, 15
	25	6, 7	0.84	24, 22
	35	8, 8	1.12	31, 29
	45	10, 10		
Rectangular (A = 25) Beam #1 Day 1	5	3, 3, 3, 3, 3	0.18	10, 9, 9, 9
			0.43	22, 21, 21, 21
	15	9, 9, 9, 9, 9	0.70	34, 32, 32, 32
	25	14, 14, 15, 15, 15		
Rectangular (A = 25) Beam #1 Day 2	5	3, 4	0.28	14, 15
	10	7, 7	0.56	27, 28
	15	9, 9	0.84	39, 39
	25	15, 15	1.12	52, 52
	35	20, 20		
Rectangular (A = 25) Beam #2	5	2	0.28	13, 13, 12, 12
	10	5	0.56	25, 24, 25, 24
	15	8	0.84	34, 34, 35, 35
	25	16	1.12	46, 45, 45, 45
	35	23		
Rectangular (A = 25) Beam #3	5	3, 3, 3	0.28	13, 11
	10	6, -, 5	0.56	23, 22
	15	8, 5, 7	0.84	33, 31
	25	14, 11, 12	1.12	43, 41
	35	16, 16, 17		
Rectangular (A = 25) Beam #4	5	2, 3	0.28	15, 14
	10	5, 5	0.56	26, 27
	15	10, 8	0.84	40, 38
	25	15, 13	1.12	53, 50
	35	16, 17		
Rectangular (A = 37.5)	5	8, 9, 8, 8	0.28	14, 14, 19, 20
	15	21, 22, 20, 22	0.56	34, 30, 36, 34
	25	34, 33, 33, 34	0.84	47, 45, -, 47
	35	47, 45, 45, 45	1.12	59, 55, 62, 60
Rectangular (A = 50)	5	13, 14, 15	0.28	19, 16, 19, 16, 17,18, 18, 18
	10	25, 28, -	0.56	36, 34, 34, 33, 34, 34, 31, 34
	15	44, 39, 41	0.84	53, 50, 49, 47, 48, 48, 50, 50
	25	66, 66, 67	1.12	66, 61, 66, 63, 65, 65, 61, 60
Trap (110, 68) (A = 25) Day 1	5	4, 4, 4, 5	0.18	10, 9, 9, 10
			0.43	23, 22, 22, 22
	15	12, 11, 11, 12	0.70	35, 34, 34, 34
	25	18, 17, 18, 19		
Trap (110, 68) (A = 25) Day 2	5	4, 4	0.28	19, 14
	10	7, 7	0.56	32, 27
	15	12, -	0.84	48, 42
	25	19, 18	1.12	64, 57
	35	27, 27		

SI_Figure 3 shows bending displacement under consecutive loading and unloading cycles. There was no sign of hysteresis, and the slopes of the eight lines varied by at most 3%. Thus, we remained in the elastic regime, and increasing or decreasing loads can be treated as equal in performing further analysis.



SI_Figure 3. Displacement versus bending load for a rectangular crenellated beam with $A = 50$ during loading and unloading. Inset: one loading-unloading cycle, with the directions indicated by arrows.

SI_Figure 4 shows the average displacement (averages of the displacements for each load for each beam from SI_Table 2) for four nominally identical rectangular crenellated structures ($A = 25$) in axial and bending loading. Beam # 1 (dotted line – linear fit) was tested on two separate days to measure repeatability after unmounting and re-mounting. The two linear fit lines overlap for axial loading and are close for bending. The stiffness of the beam is given by the inverse of the slope of the linear fit. Stiffnesses determined for beam #1 on the two different dates were within 0.04% for axial and 1.35% for bending. Thus, variation due to mounting was small.



SI_Figure 4. (a) Axial and (b) bending displacement vs. applied load for four rectangular crenellations with $A = 25$.

The standard deviations of the slopes of the four nominally identical rectangular beams were at most 12% for axial extension (SI_Figure 4a) and 10% for bending (SI_Figure 4b). Even though the structures were hand made, the data showed good reproducibility in fabrication. However, in comparison to repeated testing of the same beam on two separate days or repeated testing of a

beam several times, this error was much higher, as would be expected. Thus, the dominant error in these experiments is from the fabrication process.

SI_Table 3 shows the axial and bending stiffness values that were used the main text. Bending stiffness was normalized to the experimentally determined stiffness of the straight beam; axial stiffness values were normalized to the rectangular crenellation with $A = 25$, set to 1×10^{-4} based on the analytically-obtained ratio of this to the straight beam (see section 3.3 in the main text).

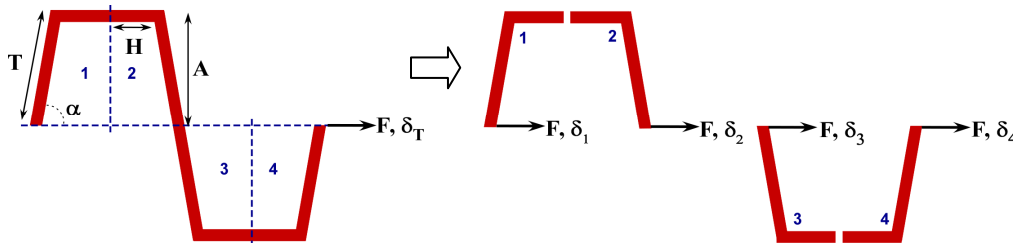
SI_Table 3. Axial and bending stiffness values calculated from the data in SI_Table 2. Standard deviations are given if multiple measurements were performed.

	k_x (N/m)	k_y (N/m)	<i>Normalized</i> k_x ($\times 10^{-4}$)	<i>Normalized</i> k_y
Beam	-	0.562		1.00
Triangular ($A = 25$)	44.05 ± 3.00	0.347 ± 0.022	2.45	0.62
Rectangular ($A = 25$)	17.98 ± 2.19	0.223 ± 0.023	1.00	0.41
Trap (110,68) ($A = 25$)	13.32 ± 0.13	0.190 ± 0.011	0.75	0.34
Rectangular ($A = 37.5$)	7.46	0.179	0.42	0.32
Rectangular ($A = 50$)	3.67	0.170	0.20	0.30

SI-4. Axial Stiffness Derivation, Detailed

The stiffness of a crenellated structure can be estimated with beam theory. The following assumptions were made in these derivations.

- The applied force is small and does not cause plastic deformation.
- The deflections are small, so the small-angle approximation, $\sin \theta \approx \theta$, can be used. (The largest deflection that the beams experienced was 10° , and even at 14° the error from using this approximation is still only 1%.)
- The beam has a uniform thickness t , a uniform width w , and an isotropic, uniform modulus E .



SI_Figure 5. Schematic of a cantilever structure with one period split into four parts.

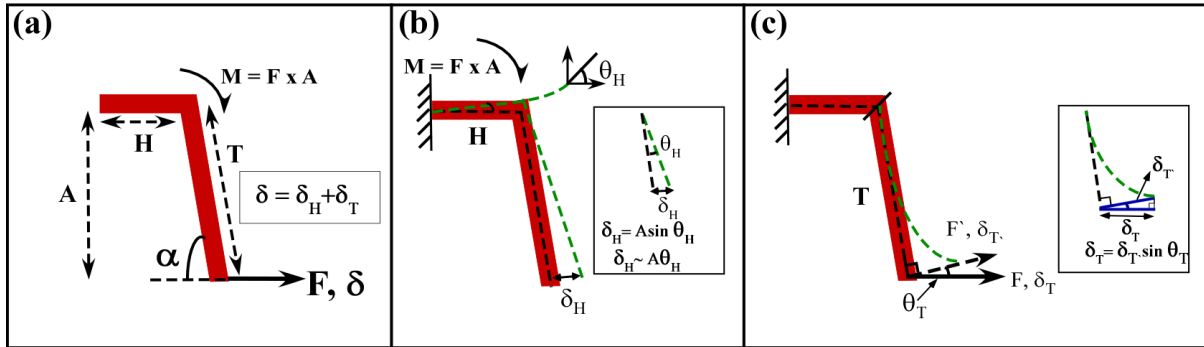
The structure can be divided into constituent parts (SI_Figure 5), each comprising a horizontal segment H and a tilted or vertical segment T. Each unit (spring) experiences the same applied force F . The total deflection of the structure is estimated to be equal to the sum of the deflections of these parts. The stiffness of the structure is given by the force divided by the total displacement, and the displacements of all the unit parts are assumed to be equal. If there are 3 periods each made up of 4 unit parts, then

$$(SI-10) \quad k_x = \frac{F}{\delta} = \frac{F}{\delta_1 + \delta_2 + \dots + \delta_{12}} = \frac{F}{12\delta} .$$

The displacement of the unit part is found by summing the displacements due to the motions of H and T.

Contribution of H

Consider first the deformation of the horizontal segment H (SI_Figure 6a). The force produces a moment $M = F \times A$ that causes H to bend, where A , the amplitude, is the distance that the horizontal segment is vertically offset from the parallel line of force. The *decrease* in the x -position of the rightmost tip of this unit due to this bending of H is relatively small and is neglected. However, the change in angle θ_H (SI_Figure 6b) at the point where H and T meet causes segment T to tilt and, thereby, to deflect in the $+x$ direction by δ_H .



SI_Figure 6. (a) The unit part under consideration. (b) Rigid body rotation of segment T due to the deformation of segment H. The axial force creates a moment M acting on H (force \times offset, $M = F \times A$), and this causes a rigid body rotation of T, producing a deflection δ_H . (c) T is treated as a cantilever beam experiencing a point load at the tip. The axial force causes a deflection δ_T . The total deflection is the sum of deflections δ_H and δ_T .

The rotation θ_H is given by [2]:

$$(SI-11) \quad \sin \theta_H \approx \theta_H = \frac{MH}{EI} = \frac{FAH}{EI} ,$$

where θ_H is given in radians, H is the length of the horizontal section, E is the Young's modulus of the material, and I is the moment of inertia. The deflection δ_H is then found using

$$(SI-12) \quad \delta_H = A \sin \theta_H \approx A \theta_H = \frac{FA^2H}{EI} .$$

Contribution of T

Consider next the bending of the tilted segment T caused by a force F at the tip (SI_Figure 6c). If a force F' is applied perpendicular to a beam of length T then the deflection is given by [2]:

$$(SI-13) \quad \delta_T = \frac{F' T^3}{3EI} .$$

The length of the tilted segment T is equal to $A/\sin\alpha$, and the force is applied not perpendicular but at an angle $\theta + 90 - \alpha$ from the perpendicular. The displacement in x is therefore the displacement perpendicular to the beam multiplied by $\sin\alpha$. The equation becomes:

$$\delta_T = \sin\alpha \frac{F \cos(\theta_H + 90 - \alpha) \left(\frac{A}{\sin\alpha} \right)^3}{3EI}$$

(SI-14)

since $F' = F \cos(\theta_H + 90 - \alpha)$.

Obtaining the Axial Stiffness

The axial stiffness is found by summing the two deflections (SI_Figure 6):

$$(SI-15) \quad \delta = \delta_H + \delta_T = \frac{FA^2H}{EI} + \sin\alpha \frac{F \cos(\theta_H + 90 - \alpha) \left(\frac{A}{\sin\alpha} \right)^3}{3EI} = \frac{FA^2}{EI} \left(H + \frac{A \cos(\theta_H + 90 - \alpha)}{3(\sin\alpha)^2} \right)$$

If the device has a rectangular cross-section, then $I = wt^3/12$, where w is the width and t is the thickness. Then k_p for the unit part equals

$$(SI-16) \quad k_p = \frac{Ewt^3}{12A^2 \left(H + \frac{A \cos(\theta_H + 90 - \alpha)}{3(\sin\alpha)^2} \right)}$$

and k_x for a structure of 12 parts is

$$(SI-17) \quad k_x = \frac{Ewt^3}{144A^2 \left(H + \frac{A \cos(\theta_H + 90 - \alpha)}{3(\sin\alpha)^2} \right)}$$

Note: because $\sin(180 - \alpha) = \sin(\alpha)$, the following two geometries (SI_Figure 7) have equivalent stiffness *if* all the horizontal segments have the same length.



SI_Figure 7. Two geometries with equivalent stiffness.

SI-5. Simplification of Bending Stiffness for Rectangular Crenellation

For a rectangular crenellation $\cos \alpha_i = 0$ for the odd-numbered terms since $\alpha_i = 90^\circ$. Equation (19) in the main paper then simplifies to:

$$\begin{aligned}
 \delta &= \frac{FT}{EI} \left\{ \left[\frac{T^2 \cos^2 \alpha_1}{3} + L_1 T \cos \alpha_1 + L_1^2 \right] + 2 \sum_{i=odd, i=3}^{4n-1} \left[\frac{(2T)^2 \cos^2 \alpha_i}{3} + 2L_i T \cos \alpha_i + L_i^2 \right] \right\} \\
 \text{(SI-18)} \quad &+ \frac{F(2H)}{EI} \sum_{i=even, i=2}^{4n} \left[\frac{(2H)^2}{3} + 2L_i H + L_i^2 \right] \\
 &= \frac{FT}{EI} \left\{ [L_1^2] + 2 \sum_{i=odd, i=3}^{4n-1} [L_i^2] \right\} + \frac{F(2H)}{EI} \sum_{i=even, i=2}^{4n} \left[\frac{(2H)^2}{3} + 2L_i H + L_i^2 \right]
 \end{aligned}$$

For $n = 3$,

$$\text{(SI-19)} \quad L_i = L - \frac{iL}{12} \quad (i = \text{even terms}) \text{ and}$$

$$\text{(SI-20)} \quad L_i = L - \frac{(i-1)L}{12} \quad (i = \text{odd terms}).$$

Substituting L_i for the odd and the even terms into Equation (SI-18) yields:

$$\begin{aligned}
 \delta &= \frac{FT}{EI} \left\{ [L_i^2] + 2 \sum_{i=odd, i=3}^{11} [L_i^2] \right\} + \frac{F(2H)}{EI} \sum_{i=even, i=2}^{12} \left[\frac{(2H)^2}{3} + 2L_i H + L_i^2 \right] \\
 \text{(SI-21)} \quad &= \frac{FT}{EI} \left\{ [L^2] + 2 \left[\left(L - \frac{2L}{12}\right)^2 + \left(L - \frac{4L}{12}\right)^2 + \left(L - \frac{6L}{12}\right)^2 + \left(L - \frac{8L}{12}\right)^2 + \left(L - \frac{10L}{12}\right)^2 \right] \right\} + \\
 &\frac{F(2H)}{EI} \left[\begin{aligned} &6 * \frac{(2H)^2}{3} + 2H \left[\left(L - \frac{2L}{12}\right) + \left(L - \frac{4L}{12}\right) + \left(L - \frac{6L}{12}\right) + \left(L - \frac{8L}{12}\right) + \left(L - \frac{10L}{12}\right) \right] \\ &+ \left(L - \frac{10L}{12}\right)^2 + \left(L - \frac{2L}{12}\right)^2 + \left(L - \frac{4L}{12}\right)^2 + \left(L - \frac{6L}{12}\right)^2 + \left(L - \frac{8L}{12}\right)^2 + \left(L - \frac{10L}{12}\right)^2 \end{aligned} \right]
 \end{aligned}$$

Further rearrangement and combination gives:

$$(SI-22) \quad \delta = \frac{FT}{EI} \left\{ \left[L^2 \right] + 2 \left[\frac{100L^2}{144} + \frac{64L^2}{144} + \frac{36L^2}{144} + \frac{16L^2}{144} + \frac{4L^2}{144} \right] \right\} + \frac{F(2H)}{EI} \left[8H^2 + 2H \left[\frac{10L}{12} + \frac{8L}{12} + \frac{6L}{12} + \frac{4L}{12} + \frac{2L}{12} \right] + \left[\frac{100L^2}{144} + \frac{64L^2}{144} + \frac{36L^2}{144} + \frac{16L^2}{144} + \frac{4L^2}{144} \right] \right],$$

and the total deflection becomes:

$$(SI-23) \quad \delta = \frac{FT}{EI} \left\{ L^2 + \frac{440L^2}{144} \right\} + \frac{F(2H)}{EI} \left[8H^2 + \frac{60L}{12} H + \frac{220L^2}{144} \right].$$

Since, for a rectangular crenellation, $T = A$ and $L = 6(2H)$, Equation (SI-23) can be simplified as follows:

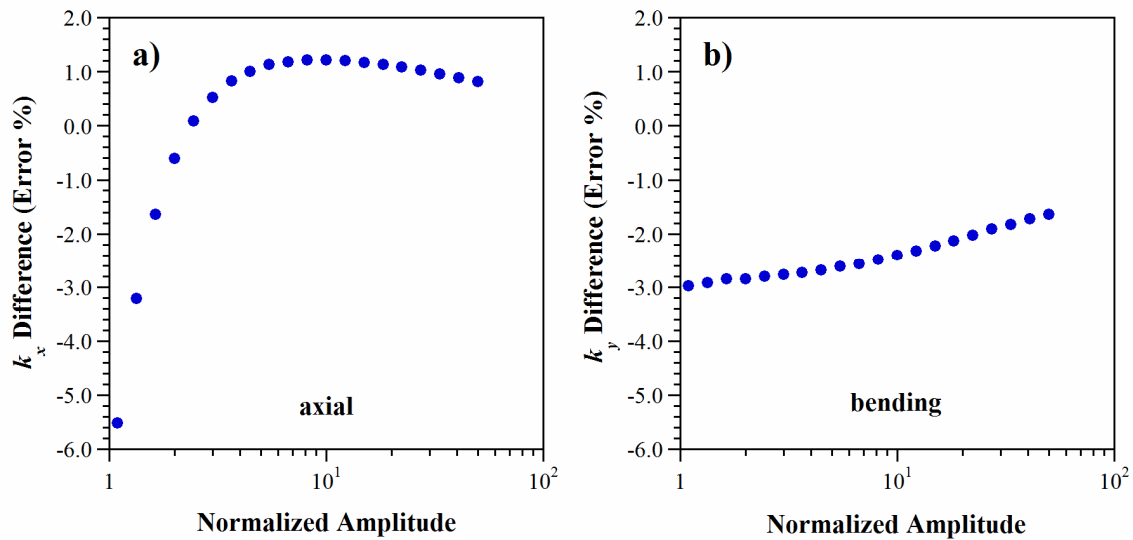
$$(SI-24) \quad \begin{aligned} \delta &= \frac{FA}{EI} \left\{ \frac{584L^2}{144} \right\} + \frac{F(2L)}{12EI} \left[\frac{8L^2}{144} + \frac{60L^2}{144} + \frac{220L^2}{144} \right] \\ &= \frac{FA}{EI} \left\{ \frac{584L^2}{144} \right\} + \frac{FL}{6EI} \left[\frac{288L^2}{144} \right] \\ &= \frac{FA}{EI} \left\{ \frac{73L^2}{18} \right\} + \frac{FL^3}{3EI} \\ &= \frac{F}{18EI} [73AL^2 + 6L^3] \end{aligned}$$

For a rectangular cross-section, $I = wt^3/12$ and $k_y = \frac{F}{\delta}$. Substituting into Equation (SI-24) yields:

$$(SI-25) \quad \begin{aligned} k_y &= \frac{18EI}{6L^3 + 73AL^3} \\ &= \frac{3Ewt^3}{2(6L^3 + 73AL^2)} \end{aligned}$$

SI-6. FEM Results vs. Analytical Estimates

The values from the FEM simulations and the analytical estimates for the axial and bending stiffnesses of the rectangular crenellated beam were shown in Figure 7a and Figure 8a of the main text. The difference in the values, $\frac{FEM - Analytical}{FEM}$, is shown as a function of amplitude in SI_Figure 8, normalized by thickness. The difference was at most 5.5% for the axial stiffness and 3% for the bending stiffness, being greatest at small amplitudes when $A \approx t$.



SI Figure 8. For the rectangular beam in Figure 7a and Figure 8a of the main text, the difference between the FEM and analytical a) axial stiffness b) bending stiffness values.

References

1. A. B. Comsol, "COMSOL multiphysics user's guide," (2005).
2. J. M. Gere and S. P. Timoshenko, Mechanics of Materials, 4th ed. (PWS Publishing Company, Boston, 1997).
3. T. A. Davis, UMFPACK version 4.4 user guide, (Department of Computer and Information Science and Engineering, University of Florida, Florida, 2005).